THESIS APPROVAL

GRADUATE SCHOOL, KASETSART UNIVERSITY

Master of Engineering (Chemical Engineering)

DEGREE

Chemical Engineering | Chemical Engineering

FIELD | **DEPARTMENT**

TITLE: Effect of Meso-Macroporous Silica Supports on Deactivation of Nickel Catalyst in Methane Cracking Reaction

NAME: Mr. Chan Tanggarnjanavalukul

THIS THESIS HAS BEEN ACCEPTED BY

THESIS ADVISOR

(Associate Professor Metta Chareonpanich, D.Eng.)

THESIS CO-ADVISOR

(Associate Professor Paisan Kongkachuichay, Ph.D.)

DEPARTMENT HEAD

(Associate Professor Apinya Duangchan, Ph.D.)

APPROVED BY THE GRADUATESCHOOL ON _____

DEAN

(Associate Professor Gunjana Theeragool, D.Agr.)

Copyright by Kasetsart University All rights reserved

THESIS

EFFECT OF MESO-MACROPOROUS SILICA SUPPORTS ON DEACTIVATION OF NICKEL CATALYST IN METHANE CRACKING REACTION

CHAN TANGGARNJANAVALUKUL

A Thesis Submitted in Partial Fulfillment of
the Requirements for the Degree of
Master of Engineering (Chemical Engineering)
Graduate School, Kasetsart University
2014

Copyright by Kasetsart University All rights reserved

Chan Tanggarnjanavalukul 2014: Effect of Meso-Macroporous Silica Supports on Deactivation of Nickel Catalyst in Methane Cracking Reaction. Master of Engineering (Chemical Engineering), Major Field: Chemical Engineering, Department of Chemical Engineering. Thesis Advisor: Associate Professor Metta Chareonpanich, D.Eng. 89 pages.

In this research, bimodal porous silica with different pore sizes (MCM-41 and BPS-5) and monomodal porous silica supports (SBA-15 and Xerogel-5) were synthesized in order to investigate the effect of pore characteristic on life time of the catalysts in methane cracking reaction. These supports were synthesized by sol-gel technique and were loaded with 5 wt.% nickel by incipient wetness impregnation method. The physicochemical properties of the obtained catalysts were examined by using N_2-sorption, X-ray diffraction (XRD), X-ray absorption spectroscopy (XAS) and temperature programmed reduction (TPR). The catalytic performance was investigated under atmospheric pressure in the temperature ranges of 500-650 °C with CH_4/N_2 molar ratio of 1:4 and total flow rate of 100 ml/min. It was found that life times of the catalysts significantly depended on the pore characteristic of supports. The largest pore size Ni/BPS-5 (174 nm) exhibited the longest life time, which was of 250 min time on stream and the highest initial methane conversion (~75%). The life time of catalysts was affected from the pore blockage of deposited carbon nanofibers which abruptly deactivated the smallest pore size Ni/Xerogel-5 (6.5 nm) within 20 min. Moreover, the higher operating temperature enhanced the graphitic order of carbon nanofibers as evident by Raman spectroscopy result.

_____ _____ __ / __ / __

Student's signature Thesis Advisor's signature

Copyright by Kasetsart University All rights reserved

ACKNOWLEDGEMENTS

I would like to take this opportunity to acknowledge the people who have helped to make this work possible. My sincere gratitude first goes to my thesis advisor Associate Professor Dr. Metta Chareonpanich, for her consistent and thoughtful advice, continuous encouragement and help during the course of this work. Moreover, I am grateful to my graduate committees, Dr. Thongthai Witoon, and Associate Professor Dr. Paisan Kongkachuichay for their kindly giving the time to advice, revise and approve my thesis.

I gratefully acknowledge the financial support from Center of Advanced studies in Nanotechnology and its Applications in Chemical, Food and Agricultural Industries, Kasetsart University, the National Science and Technology Development Agency (NSTDA Chair Professor and NANOTEC Center of Excellence), and the Kasetsart University Research and Development Institute (KURDI). I also would like to thank the Synchrotron Light Research Institute (Public Organization) for their support my results.

I am grateful to my fellow graduate students at Department of Chemical Engineering, Kasetsart University for assisting me my research and offering valuable suggestion.

Finally, I would like to thank my family for their love, support, encouragement, and their understanding during the whole period of my education. My family has been my greatest source of strength and inspiration. My gratefulness devotes to my family who wholeheartedly support me away.

Chan Tanggarnjanavalukul

May 2014

Copyright by Kasetsart University All rights reserved

TABLE OF CONTENTS

Page

TABLE OF CONTENTS	i
LIST OF TABLES	ii
LIST OF FIGURES	iii
INTRODUCTION	1
OBJECTIVES	3
LITERATURE REVIEW	4
MATERIALS AND METHODS	29
RESULTS AND DISCUSSION	42
CONCLUSIONS	65
LITERATURE CITED	66
APPENDICES	77
Appendix A Qualitative and quantitative results from gas chromatography	78
Appendix B Conversion and Yield results	81
Appendix C Diameter of crystallite nickel oxide calculation	84
Appendix D Effective Diffusion Coefficient Calculation	86
CIRRICULUMVITAE	89

Copyright by Kasetsart University All rights reserved

LIST OF TABLES

Table		Page
1	Summary of the experiments conducted	24
2	Physical properties of porous silica supports and catalysts.	46
3	H_2 uptake of Ni catalysts supported on different supports.	52
4	Methane diffusivity in pore of Ni catalysts supported on different supports	64

Appendix Table

A1	Equation of calibration curves for standard gas	80
B1	Example of conversion and yield of methane cracking reaction over Ni/BPS-5	83

Copyright by Kasetsart University All rights reserved

LIST OF FIGURES

Figure		Page
1	The classical mechanism of carbon filament formation scheme.	5
2	Schematic representation of the deformation of the metal particle (a) formation of full filaments and (b) formation of hollow filaments.	6
3	Methane conversion over Ni/SiO_2 at 600 ^oC (■), 550 ^oC (●) and 500 ^oC (▲).	7
4	SEM images of 5 wt% $Ni/\gamma\text{-}Al_2O_3$ catalyst after (a) 14 h reaction at 650 °C, (b) 13 h reaction at 600 °C, (c) 8 h reaction at 550 °C and (d) 16 h reaction at 500 °C.	8
5	Methane decomposition over $Ni/MgAl_2O_4$ catalyst at temperature of 550 ^oC with differentN_2:CH_4 molar ratios.	9
6	Effect of the CH_4 flow rate on the hydrogen production and CH_4 conversion: run 5:20 ml/min; run 7:50 ml/min; run 6:100 ml/min.	10
7	Methane conversion over different nickel content supported on SiO_2 catalysts at 600 °C.	11
8	Methane conversion over (a) NCB and (b) Ni/NCB and Co/NCB catalysts at 850 ^oC.	12
9	Hydrogen content (% vol.) in the product gases. Operating conditions: 700 °C and 12 Ndm^3 $CH_4 \cdot (h \cdot gcat)^{-1}$ for the Ni-based catalysts and 800 °C with 1.5 Ndm^3 $CH_4 \cdot (h \cdot gcat)^{-1}$ for the Fe-based catalysts.	13
10	Effect of reaction temperature on the amount of carbon deposited over nine transition metals loaded on MgO.	14

Copyright by Kasetsart University All rights reserved

LIST OF FIGURES (Continued)

Figure		Page
11	Hydrogen evolution in reactor tests at 700 °C with the Ni/TiO_2 and $Ni–Cu/TiO_2$ catalysts prepared by impregnation and fusion method.	16
12	Effect of the calcination temperatures on the hydrogen yield (a) Ni-Al catalysts. (b) Ni-Cu-Al catalysts.	17
13	H_2 formation rate of methane decomposition over different preparation method of the Ni/CeO_2 catalyst at reaction temperature of 500 ^oC.	18
14	Methane conversion in the methane decomposition over Ni catalysts loaded on different supports at 500 ^oC.	19
15	Ni K-edge XANES spectra of supported-Ni catalysts, NiO and Ni foil.	20
16	Methane conversion in methane decomposition at temperature of 500 ^oC over Co catalysts loaded on different supports.	21
17	(a) Temperature programmed reaction of CH_4 (TPCR) over Ni supported catalysts (CRG-F is a commercial steam reforming catalyst) (b) reaction rate as a function of Ni dispersion in isothermal conditions.	22
18	Methane conversion during methane decomposition over 30 wt% Ni supported catalysts at 550 ^oC.	23
19	Polymerization behavior of silica: In acid solution or in presence of flocculating salts (A), particles aggregate into three-dimensional networks and form gels; In basic solution (B) particles in sol grow in size with decrease in numbers.	26
20	TEM image of meso-macro porous silica with adjusting pH: (a) pH = 2 and (b) pH = 3 (c) pH = 5.	27

Copyright by Kasetsart University All rights reserved

LIST OF FIGURES (Continued)

Figure		Page
21	Catalytic reaction testing unit: (a) a feed flow measuring and controlling system, (b) a furnace-equipped inconel-600 tube reactor and (c) a sampling system.	37
22	Mass flow controller: (a) Aalborg GFC thermal mass flow controller and (b) KOFLOC mass flow controller and mass flow meter with indicator.	38
23	The reactor of methane cracking reaction equipped with the electric heater (Carbolite tube furnace).	39
24	Schematic setup of the stage of methane cracking reaction reactor.	39
25	Shimadzu gas chromatograph (GC-2014) equipped with thermal conductivity detector (TCD) and chromatopac data processor.	40
26	Adsorption-desorption isotherm of (A) porous silica supports (a) SBA-15 (b) Xerogel-5 (c) MCM-41 and (d) BPS-5 and (B) nickel loaded on porous silica supports (a) Ni/SBA-15 (b) Ni/Xerogel-5 (c) Ni/MCM-41 and (d) Ni/BPS-5.	43
27	Pore size distribution of (A) porous silica supports: (a) SBA-15 (b) Xerogel-5 (c) MCM-41 and (d) BPS-5, and (B) nickel loaded on porous silica supports: (a) Ni/SBA-15 (b) Ni/Xerogel-5 (c) Ni/MCM-41 and (d) Ni/BPS-5.	45
28	Small angle X-ray scattering (SAXS) patterns of porous silica supports. (a) SBA-15 (b) Xerogel-5 (c) MCM-41 and (d) BPS-.5	48
29	XRD patterns of 5 wt.% Ni on porous silicas supports. (a) Ni/SBA-15 (b) Ni/Xerogel-5 (c) Ni/MCM-41 and (d) Ni/BPS-5.	49
30	TPR curves of (a) NiO/SBA-15, (b) NiO/Xerogel-5, (c) NiO/MCM-41, and (d) NiO/BPS-5 —— TPR profile from experiment - - - TPR profile from program ····· Deconvoluted NiO profile	51

Copyright by Kasetsart University All rights reserved

LIST OF FIGURES (Continued)

Figure		Page
31	Ni K-edge XANES spectra of nickel on silica supports, NiO and Ni foil (A) fresh nickel catalysts (a) standard NiO (b) Ni/SBA-15 (c) Ni/Xerogel-5 (d) Ni/MCM-41 and (e) Ni/BPS-5 and (B) nickel catalyst reduced at 600 ^{o}C (a) Ni foil (b) Ni/SBA-15 (c) Ni/Xerogel-5 (d) Ni/MCM-41 and (e) Ni/BPS-5.	53
32	CH_4 conversion in the CH_4 cracking over Ni catalysts supported on different supports at (a) 500 ^{o}C (b) 550 ^{o}C (c) 600 ^{o}C and (d) 650 ^{o}C —▲— Ni/SBA-15 ···△··· Ni/Xerogel-5 —■— Ni/MCM-41 ··□·· Ni/BPS-5	55
33	H_2 yield in the CH_4 cracking over Ni catalysts supported on different supports at (a) 500 ^{o}C (b) 550 ^{o}C (c) 600 ^{o}C and (d) 650 ^{o}C —▲— Ni/SBA-15 ···△··Ni/Xerogel-5 —■— Ni/MCM-41 ··□·· Ni/BPS-5	56
34	SEM images of Ni catalysts supported on different supports after the complete deactivation by the methane cracking at 500 ^{o}C.	58
35	TGA curves of catalysts after CH_4 cracking reaction at (a) 500 ^{o}C (b) 550 ^{o}C (c) 600 ^{o}C and (d) 650 ^{o}C. – – Ni/SBA-15 - - - - Ni/Xerogel-5 —— Ni/MCM-41 —— Ni/BPS-5	59
36	DTA curves of catalysts after CH_4 cracking reaction at (a) 500 ^{o}C (b) 550 ^{o}C (c) 600 ^{o}C and (d) 650^{o}C. – – Ni/SBA-15 - - - - Ni/Xerogel-5 —— Ni/MCM-41 —— Ni/BPS-5	60
37	Raman spectra of catalysts after CH_4 cracking reaction at (A) 500 ^{o}C and (B) 650 ^{o}C (a) Ni/SBA-15 (b) Ni/Xerogel-5 (c) Ni/MCM-41 and (d) Ni/BPS-5	62

Copyright by Kasetsart University All rights reserved

LIST OF FIGURES (Continued)

Appendix Figure		Page
A1	Schematic diagram of gas chromatograph	79

Copyright by Kasetsart University All rights reserved

EFFECT OF MESO-MACROPOROUS SILICA SUPPORTS ON DEACTIVATION OF NICKEL CATALYST IN METHANE CRACKING REACTION

INTRODUCTION

Recently, H_2 is widely used in chemical process industry, electronics, food processing and metal manufacturing and moreover, H_2 is a promising fuel in the automotive sector (Zapata *et al.,* 2010; Awadallah *et al.,* 2014). Due to the fact that hydrogen is a clean energy with the highest energy per unit weight, the annual global hydrogen consumption is therefore gradually increased (Nuernberg *et al.,* 2008). Accordingly, methane is concerned as one of preferred sources for hydrogen production because of its availability, low cost, and high ratio of hydrogen to carbon (Poirier *et al.,* 1997) and moreover, it is concerned as a greenhouse gas that causes global warming problem. The use of methane for hydrogen production can therefore potentially reduce the green house gas and simultaneously produced renewable energy. There are many processes which applicable to produce hydrogen from methane such as methane steam reforming (MSR), partial oxidation of methane (POM) and methane cracking reaction (Choudhary *et al.,* 2001; Echegoyen *et al.,* 2007). Methane cracking reaction can perform in lower temperature range when compared to the MSR and POM and produces CO-free hydrogen (Muradov, 2001). Moreover, methane cracking produces a significant amount of carbon filaments which have wide industrial applications such as functional materials (carbon fiber, graphite and carbon black), catalyst and adsorbents for hydrogen and electrode (Steinfeld *et al.,* 1997; Muradov *et al.,* 2005; Pinilla *et al.,* 2012). Therefore, many attempts have been focused on methane cracking reaction (Aiello *et al.,* 2000; Alstrup, 1998).

Due to the fact that catalyst supports have significant role on catalytic reaction as they help increase catalyst distribution and activities of catalysts while minimize catalyst sintering (Amin *et al.,* 2012). However, catalyst deactivation is rapidly occurred during methane cracking reaction due to carbon deposited on catalyst

Copyright by Kasetsart University All rights reserved

surface. Therefore, we expected that catalyst support modification could help lessen the catalyst deactivation.

Accordingly, silica (SiO_2) is selected to use as the catalyst support for methane cracking its less interaction between metal and support, resulting in ease of reduction compared to other supports (Takenaka *et al.,* 2001). Furthermore, nickel metal is widely used as catalyst in methane cracking reaction due to its low cost and high activity (Shaikhutdinov *et al.,* 1995; Ermakova *et al.,* 1999; Otsuka *et al.,* 2000). Therefore, nickel supported on silica was applied as the catalyst in methane cracking reaction. In many researches, it was found that the activity of nickel supported on high porous silica was more than nickel supported on less porous silica (Ermakova *et al.,* 2000). However, the pore of silica was potentially blocked by carbon filaments produced as the by-products from methane decomposition, lending to the deactivation of catalyst.

Based on the hypothesis that the small pores of bimodal porous support will help increase metal dispersion while large pores help increase the diffusion rate (Sahin *et al.,* 2003; Takahashi *et al.,* 2007). Accordingly, bimodal porous supports containing two different pore sizes were synthesized in order to improve the life time of catalyst. The bimodal porous catalysts can be simply prepared by impregnating metal oxide sols into silica gel (Shinoda *et al.,* 2004). The other technique for bimodal porous silica preparation is sol-gel method with specific templates such as chitosan (Witoon *et al.,* 2008), hyperbranched polyester H20M (Zhao *et al.,* 2006), and cetyltrimethyl ammonium bromide (CTAB) (Morales *et al.,* 2005).

In this research, silica supports with different porous structures were prepared by sol-gel method. Then, nickel precursor of 5 wt.% was loaded onto the porous silica supports. The effects of reaction temperature and pore structure of catalyst supports on catalyst deactivation in methane cracking reaction were investigated. Moreover, the structure of carbons formed on catalyst surface by methane cracking was also investigated.

Copyright by Kasetsart University All rights reserved

OBJECTIVES

1. To synthesize bimodal porous silica supports with mesopore and macropore.

2. To study the effect of pore characteristic of silica support on the performances of methane cracking reaction.

3. To study the effect of operating temperature on methane cracking reaction.

Scope

1. The catalysts and supports were prepared by incipient wetness impregnation and sol-gel techniques, respectively.

2. Methane cracking reaction was tested in packed bed reactor with CH_4/N_2 molar ratio of 1:4, total flow rate of 100 ml/min, and temperature of 500-650 ^oC.

3. Methane conversion and hydrogen yield of methane cracking reaction were investigated.

Benefits

1. Bimodal porous silica can be successfully synthesized by sol-gel method.

2. Long life time of nickel on bimodal porous silica with mesopore and macropore in methane cracking reaction was obtained.

3. High catalytic stability of low operating temperature in methane cracking reaction was achieved.

Copyright by Kasetsart University All rights reserved

LITERATURE REVIEW

Methane cracking reaction is a well-known reaction for producing hydrogen and carbon filament, however, a major problem found in the methane cracking reaction was the catalyst deactivation due to carbon deposition on the catalyst surface (Zhang and Amiridis, 1998). Therefore, this research focuses on the development of silica support to lessen the deactivation problem caused by coke deposition. The literature reviews of methane cracking reaction, the metal catalysts, catalyst preparation, supported catalysts, and the synthesis process of bimodal and monomodal porous silicas are reviewed in the details shown below.

1. Methane cracking reaction

Methane cracking reaction is the most interesting reaction for hydrogen production because it is moderately endothermic and does not produce CO or CO_2 according to the following reaction: (Malaika *et al.,* 2010; Nuernberg *et al.,* 2012)

$$CH_{4(g)} \rightarrow C_{(s)} + 2H_{2(g)} \qquad \Delta H = 75.6 \text{ kJ/mol} \qquad (1)$$

Additionally, the by-product obtained from methane cracking reaction is carbon nanomaterials (CNMs) practically used as a filler or construction material, leading to possibility to reduce the cost of hydrogen produced by marketing the carbon (Muradov *et al.,* 2006; Li *et al.,* 2000). For non-catalytic methane cracking reaction, the higher temperature as 1200 ^{o}C is required (Abbas and Daud, 2010). Thus, the metal catalyst is used in order to catalytically decompose methane to produce hydrogen at the lower temperature which depends on the catalyst type.

Typically, the reactors used for methane cracking reaction are packed-bed reactor (PBR) and fluidized-bed reactor (FBR). However, the problem of PBR is the pressure drop and the increase in the size of catalyst particles due to depositing of carbon over the catalyst surface which results in blocking the reactant gas flow

Copyright by Kasetsart University All rights reserved

(Aiello *et al.,* 2000). For FBR, the constant flow of solids through the reaction zone is difficult to control for lab-scale (Lee *et al.,* 2004).

In general, the methane cracking reaction is occurred from the decomposition of methane on the metal surface (at the active site) to form carbon and hydrogen products. After that, the deposited carbon would dissolve in the metal catalyst and form as a uniform concentration solution of carbon in the metal surface. The carbon would diffuse through the metal particle to the metal-support interface until the carbon solution in the metal is super-saturated, and then the nucleation of filament carbon begins. The mechanism is shown in Figure 1 (Snoeck *et al.,* 1997; Yang and Chen, 1989).

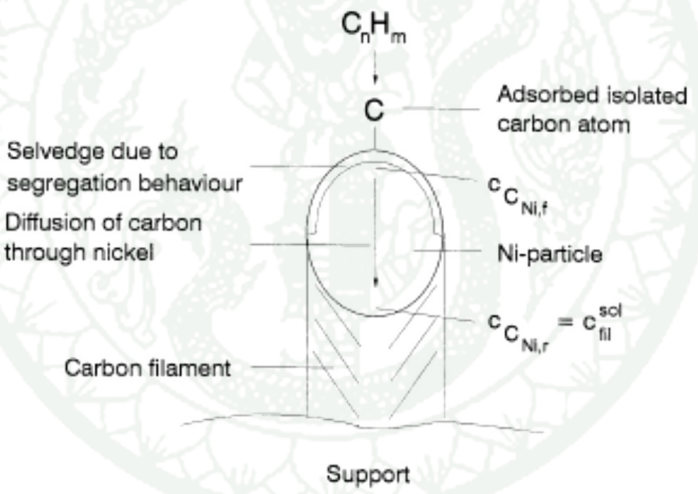

Figure 1 The classical mechanism of carbon filament formation scheme.

Source: Snoeck *et al.* (1997)

Yang and Chen (1989) reported that the carbon nanofilaments were obtained when there were the concentration gradient of carbon and temperature gradient between the gas/metal and metal/support interfaces. Kock *et al.* (1985) proposed the nucleation mechanism of carbon filament formation over 50 wt.% Ni/SiO_2. The first step for carbon filament growth was started from the carburization of deposited carbon to form nickel carbide, as shown in Equation (2):

Copyright by Kasetsart University All rights reserved

$$3Ni_{(s)} + CH_{4(g)} \rightarrow Ni_3C_{(s)} + 2H_{2(g)} \quad (2)$$

Then, nickel carbide was decomposed and started the nucleation of graphite. After that, graphite was precipitated at the nickel-support interface and detached the nickel particle from the support.

Snoeck *et al.* (1997) reported that the obtained structure of carbon filaments was depended on the reaction temperature. At low temperature, the carbon filaments without hollow channel were formed because the nucleation rate was lower than the rate of carbon diffusion through the nickel particle. Moreover, the nucleation was more uniform at the metal-support interface, therefore, the carbon filaments without hollow channel were formed as shown in Figure 2(a). On the other hand, at high temperature, the nucleation rate was faster than the diffusion rate and the distortion of nickel particles was observed. As a result, the hollow carbon filaments were formed as shown in Figure 2(b).

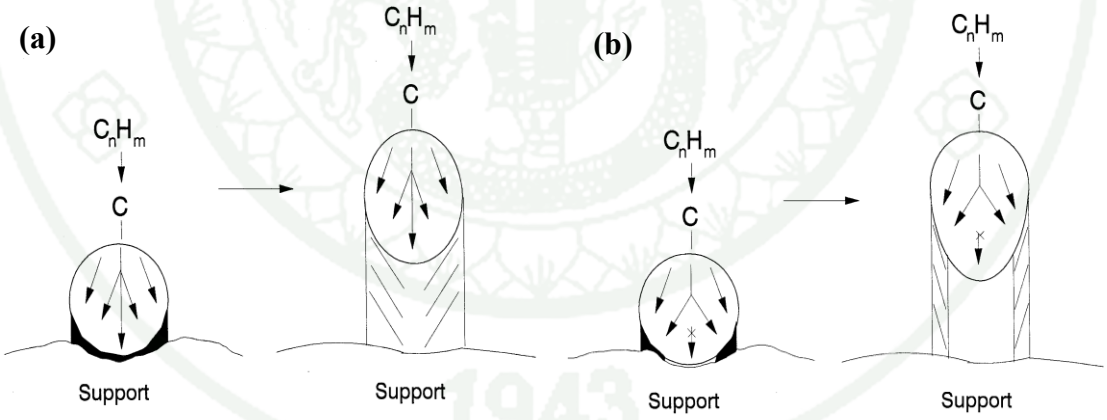

Figure 2 Schematic representation of the deformation of the metal particle (a) formation of full filaments and (b) formation of hollow filaments.

Source: Snoeck *et al.* (1997)

Ermakova *et al.* (2000) investigated the effect of the reaction temperature in methane cracking reaction by using Ni as the catalyst, and silica, alumina, magnesia

Copyright by Kasetsart University All rights reserved

and zirconium as the textural promoters. The high stability of catalyst was obtained at the temperatures range of 500-550 °C as shown in Figure 3. However, the operation at high temperature (600 ^{o}C) was inappropriate because the methane conversion was rapidly decreased. At this temperature, the rate of carbon deposition was higher than the rate of surface carbon migration and diffusion. Therefore, carbon could grow on both sides of the nickel cluster and encapsulate the nickel cluster, led to lower the catalyst stability. Moreover, the maximum methane conversion was obtained at 552 °C. At this temperature, the rate of carbon deposition on nickel particle was in equilibrium with the rate of surface carbon migration and diffusion through the nickel particle (Bokx *et al.,* 1985).

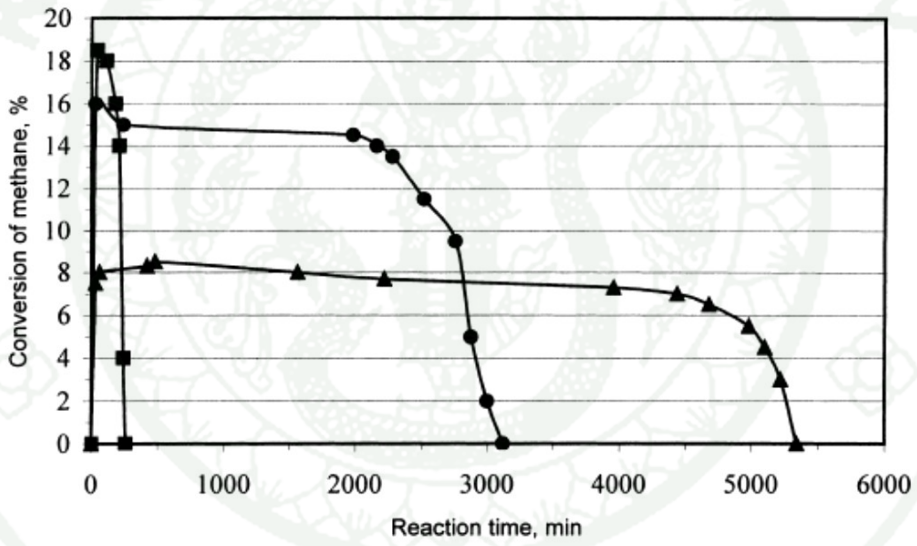

Figure 3 Methane conversions over Ni/SiO_2 at 600 ^{o}C (■), 550 ^{o}C (●), and 500 ^{o}C (▲).

Source: Ermakova *et al.* (2000)

Rahman *et al.* (2006) studied the influence of reaction temperature to the structure of carbon filaments with 5 wt.% Ni/γ-Al_2O_3 catalyst through methane decomposition. The results indicated that the carbon filaments formed on the deactivated catalyst had a little and short length at reaction temperature of 650 ^{o}C due

Copyright by Kasetsart University All rights reserved

to a rapid deactivation of the catalyst, as shown in Figure 4(a). At the lower temperatures (600, 550, and 500 ^{o}C), the quantity and length of the carbon were higher and the diameter of carbon filaments were decreased when the reaction temperature was increased, as shown in Figure 4.

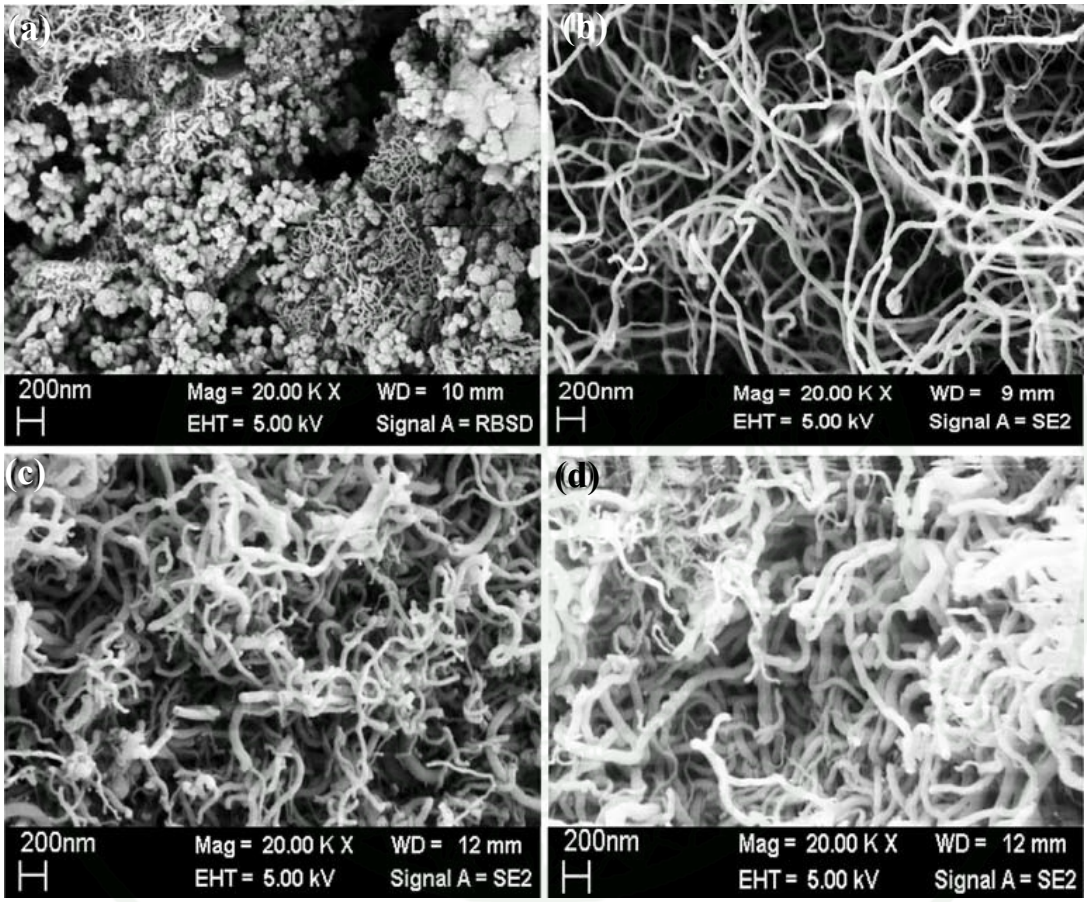

Figure 4 SEM images of 5 wt% Ni/γ-Al_2O_3 catalyst after (a) 14 h reaction at 650 °C, (b) 13 h reaction at 600 °C, (c) 8 h reaction at 550 °C and (d) 16 h reaction at 500 °C.

Source: Rahman *et al.* (2006)

Nuernberg *et al.* (2012) studied the effect of N_2:CH_4 molar ratio on methane decomposition by using Ni/$MgAl_2O_4$ as the catalyst at the temperature of 550 ^{o}C. Figure 5 shows that the N_2:CH_4 molar ratio of 7:1 with the total flow rate of 80

Copyright by Kasetsart University All rights reserved

ml/min gave the highest average methane conversion (31%) and the highest initial conversion (37%). The average and initial methane conversion were decreased when the N_2:CH_4 molar ratio was decreased. It could be explained that the amount of active sites in this catalyst was not sufficient to convert all of the methane molecules into products as increasing the methane concentration. In addition, multiwall carbon nanotubes were formed in the methane decomposition over $Ni/MgAl_2O_4$.

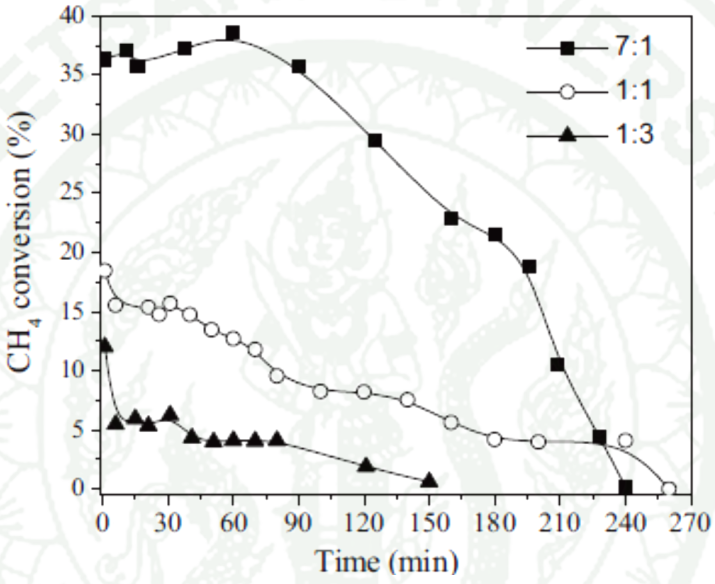

Figure 5 Methane decomposition over $Ni/MgAl_2O_4$ catalyst at temperature of 550 ^oC with different N_2:CH_4 molar ratios.

Source: Nuernberg *et al.* (2012)

Suelves *et al.* (2005) studied the effect of methane flow rate on the catalyst deactivation of methane decomposition reaction at the reaction temperature of 700 ^oC. The commercial 65 wt.% Ni supported on a mixture of silica and alumina was used as the catalyst. Figure 6 shows that the life time of the catalyst was decreased when the methane flow rate was increased. At 100 ml/min, the catalyst was completely deactivated in a short time period (~100 min). Moreover, the weights of carbon deposited per gram of used catalyst at the methane flow rate of 20, 50 and 100 ml/min were 6.3, 7.0, and 3.3 g_{carbon}/g_{cat}, respectively.

Copyright by Kasetsart University All rights reserved

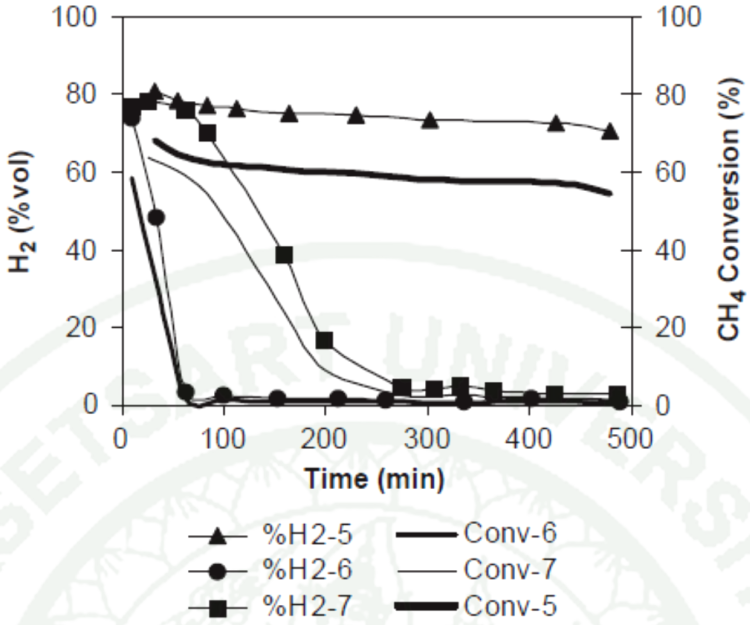

Figure 6 Effect of CH_4 flow rate on hydrogen production and CH_4 conversion: run 5:20 ml/min; run 7:50 ml/min; run 6:100 ml/min.

Source: Suelves *et al.* (2005)

2. Catalysts for methane cracking reaction

Many researchers reported that transition metal catalysts normally used in methane cracking reaction were Fe, Ni, and Co (Lee *et al.,* 2004; Avdeeva *et al.,* 1999). The obtained carbons from catalytic methane cracking reaction had various types, such as encapsulating carbons (Zhang and Smith, 2004), carbon nanotubes (CNT) (Niu and Fang, 2007), and carbon nanofibers (CNF) (Ichioka *et al.,* 2007). From the mentioned catalysts, nickel catalyst was widely used because of its low cost and relatively high activity (Shaikhutdinov *et al.,* 1995; Otsuka *et al.,* 2000), while Fe became active at a relatively higher temperature (Wang *et al.,* 2012). Among these metal catalysts, Co had lower stability for carbon than Ni (Ermakova *et al.,* 2000).

Venugapol *et al.* (2007) examined the effect of nickel content on methane conversion by loading 5-90 wt.% nickel on the silica support. The result shows that

Copyright by Kasetsart University All rights reserved

the increase of nickel amount gave a positive effect to the methane conversion and the catalyst stability until the loading amount reached 30 wt.%. From Figure 7, the methane conversion and stability were quite low with more than 30 wt.% of nickel due to the agglomeration of Ni metal particles in the preparation period. In addition, the catalyst activity was not a linear function of the nickel amount on the support.

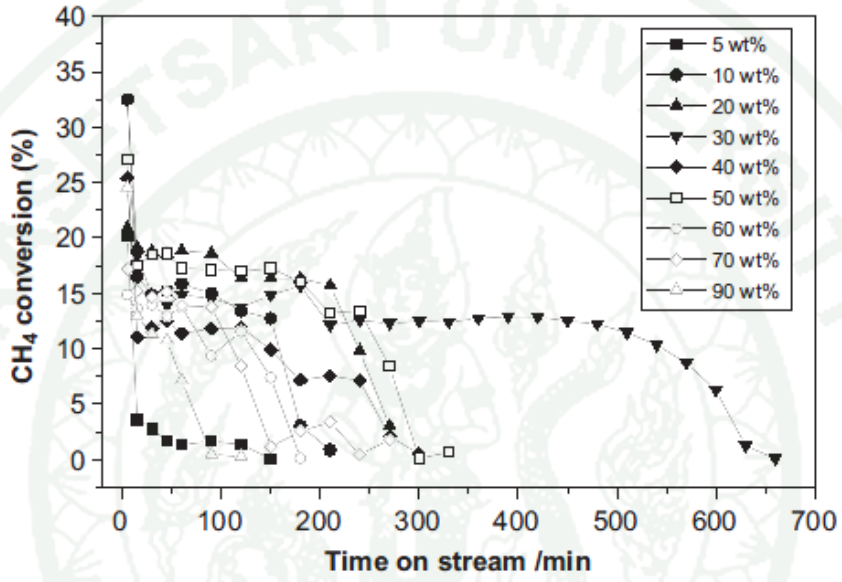

Figure 7 Methane conversions over different nickel contents supported on SiO_2 catalysts at 600 °C.

Source: Venugopal *et al.* (2007)

Zhang and Smith (2004) studied the deactivation rate of catalyst through methane decomposition at the temperature of 500 ^{o}C over Co and Ni catalysts. They found that the Ni-based catalysts were more active and stable than Co-based catalysts under the same reaction conditions because Ni-based catalysts had larger metal particle size than that of Co-based catalysts. The larger metal particle size was, the more carbon filament formation and stable activity obtained, because the smaller metal particle size could lead to encapsulating carbon formation. Moreover, they studied the effect of H_2/CH_4 ratio of the feed composition. When the carbon formation

Copyright by Kasetsart University All rights reserved

threshold ($K_M = (P_{H2})^2/P_{CH4}$) was increased, the catalyst activity and deactivation rate decreased.

Chen *et al.* (2009) used the nanosized carbon black (NCB) as catalyst for methane decomposition to produce hydrogen. The reaction was carried out in fluidized-bed reactor at temperature of 850 ^oC with the CH_4/N_2 molar ratio of 1:5 and the total flow rate of 540 ml/min. The catalytic performances of NCB before and after treatment in nitric acid were shown in Figure 8(a). It was found that the initial methane conversion of the treated NCB was 0.8 % higher than untreated NCB, while the deactivation rate of the treated NCB catalyst was faster than the untreated one. In order to increase the activity of NCB after treatment, Ni and Co metal were loaded on the NCB. After loading a small amount of Ni and Co, the initial methane conversion was increased to 6.6% and 5.6%, respectively (Figure 8(b)) but the activity was still rapidly deceased during the methane decomposition reaction.

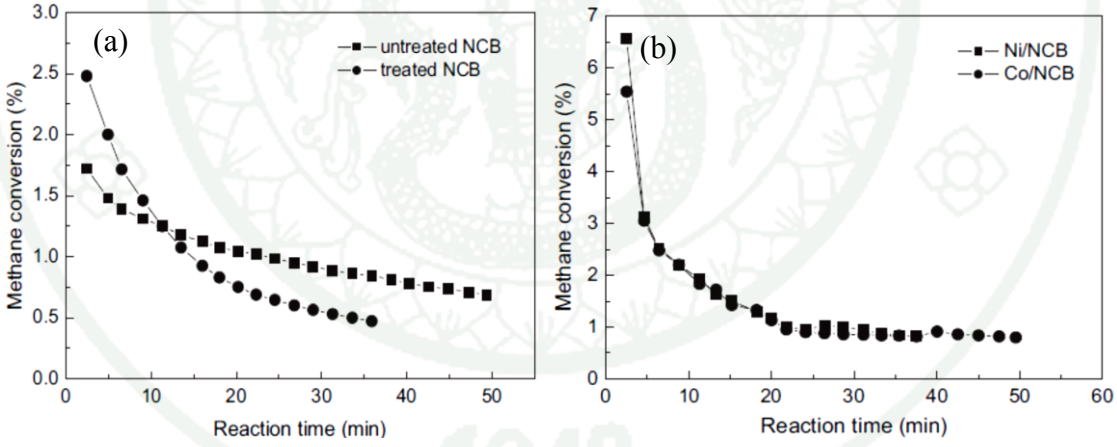

Figure 8 Methane conversions over (a) NCB and (b) Ni/NCB and Co/NCB catalysts at 850 ^oC.

Source: Chen *et al.* (2009)

Pinilla *et al.* (2011) used Ni, Ni:Cu, Fe, and Fe:Mo as the metal catalysts and Al_2O_3 and MgO as the textural promoters which prepared by using the fusion technique. The catalytic methane decomposition reaction was tested in a rotary bed

Copyright by Kasetsart University All rights reserved

reactor at the temperature of 700 °C with WHSV of 12 $Ndm^3CH_4 \cdot (h \cdot g_{cat})^{-1}$ for the Ni-based catalysts, and 800 °C with WHSV of 1.5 $Ndm^3CH_4 \cdot (h \cdot g_{cat})^{-1}$ for the Fe-based catalysts. The catalytic activity of Fe-based catalysts was lower than Ni-based catalyst and high methane conversion was obtained with the Fe-based catalysts when WHSV was decreased. Figure 9 shows the hydrogen concentration of product gases during methane decomposition reaction. It was observed that the stability of Ni-based catalysts was greater than Fe-based catalysts. The H_2 yields of 69 and 76% were obtained by using $Ni:Al_2O_3$ and Ni:Cu:MgO, respectively. However, at the beginning of methane decomposition reaction, the Fe-based catalysts show better H_2 yields (~90 %) than Ni-based catalysts.

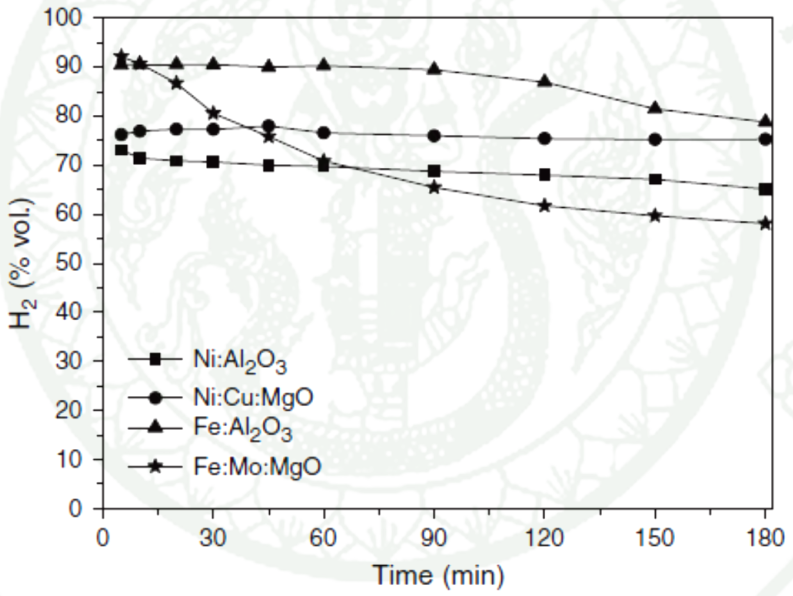

Figure 9 Hydrogen content (% vol.) in the product gases. Operating conditions: 700 °C and 12 Ndm^3 $CH_4 \cdot (h \cdot gcat)^{-1}$ for the Ni-based catalysts and 800 °C with 1.5 Ndm^3 $CH_4 \cdot (h \cdot gcat)^{-1}$ for the Fe-based catalysts.

Source: Pinilla *et al.* (2011)

Ichioka *et al.* (2007) found that several types of metal loaded on MgO catalysts could be active for the formation of carbon nanotubes (CNTs) through the chemical vapor deposition (CVD) of methane in the temperature range of 600 °C to

Copyright by Kasetsart University All rights reserved

1000 °C. The nine metal catalysts (Fe, Co, Ni, Ru, Rh, Pd, Os, Ir, and Pt) were prepared by an impregnation method. The amounts of carbon depositing on these metal catalysts in each reaction temperature within an hour were shown in Figure 10. The highest carbon deposition was obtained when Ir catalyst was used at the reaction temperature of 1000 ^{o}C (Figure 10). The higher temperature was, the more amounts of carbon was obtained. Moreover, the amounts of carbon were increased in the following order: first < second < third row transition series in the group 8-10 elements. The first row transition metal catalysts (Fe, Co, and Ni) produced small amounts of carbon. The second row transition metals generated the highest amounts of carbon when Pd catalyst was used, because the particle size of Pd was larger than those of Ru and Rh catalysts. For the third row transition metals, the highest amount of carbon was obtained at reaction temperature of 1000 ^{o}C.

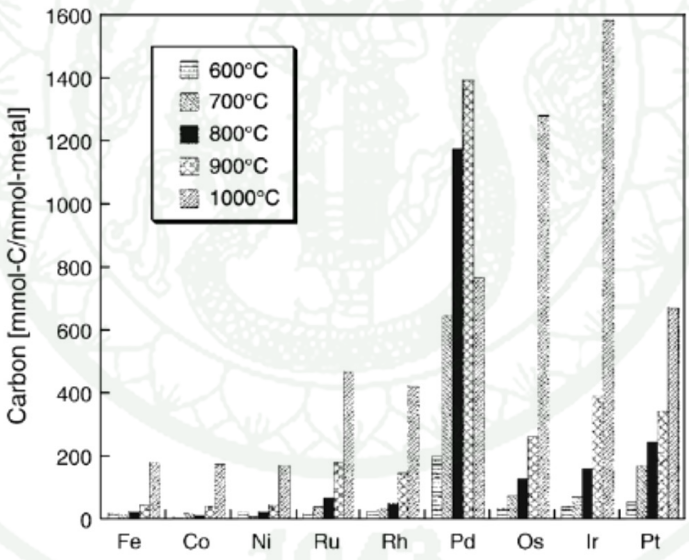

Figure 10 Effect of reaction temperature on the amount of carbon deposited over nine transition metals loaded on MgO.

Source: Ichioka *et al.* (2007)

Copyright by Kasetsart University All rights reserved

3. Catalyst preparation

There are many techniques for synthesizing catalyst used in methane cracking reaction. For example, deposition–precipitation, impregnation, sol–gel, co-precipitation, and fusion techniques have been applied for producing active and stable catalysts for catalytic methane decomposition reaction. The different preparation techniques resulted in different properties of the catalysts, such as particle size, metal distribution, and metal-support interaction. Among these techniques, impregnation and co-precipitation technique are most widely used. Moreover, the calcination temperature also affected the catalyst properties which led to different catalytic performance.

Lázaro *et al.* (2008) also studied the effect of catalyst preparation method on the catalytic cracking reaction of methane. Nickel was loaded on TiO_2 by using impregnation and fusion techniques. The results showed that the impregnation method exhibited the high initial hydrogen yield up to 80 % (Imp NiTi), as shown in Figure 11. After that the catalytic activity was rapidly decreased to a stable value at hydrogen yield of 40 %, while the fusion method (Fus NiTi – in Figure 11), was be able to keep a hydrogen yield over 60 % approximately. In addition, Cu doped in the catalysts could help increase the hydrogen yield because Cu possibly changed the reducibility of Ni through the formation of a mixed oxide during the calcination or help enhance the methane chemisorption and growth of carbon filaments. In the case of the impregnation method (Imp1 NiCuTi and Imp2 NiCuTi), the hydrogen yields were different because of the type of copper precursor used in the catalyst preparation (copper nitrate in Imp1 and copper oxide in Imp2).

Copyright by Kasetsart University All rights reserved

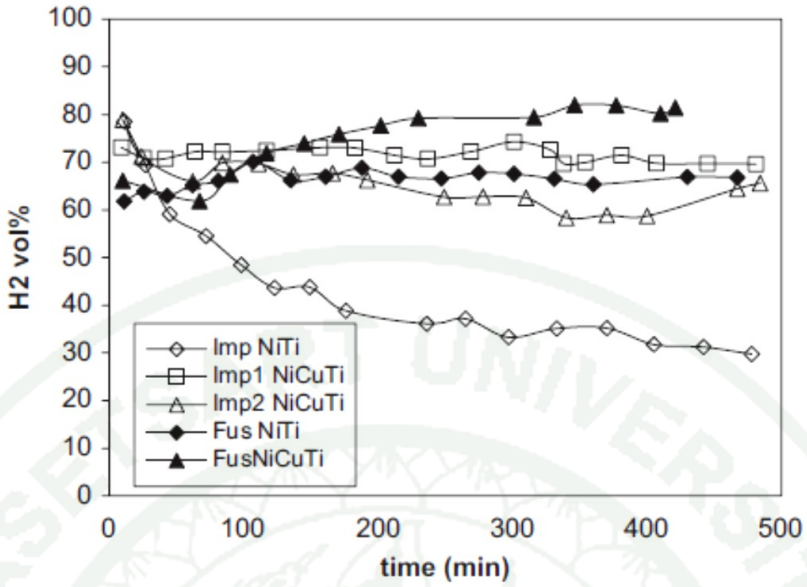

Figure 11 Hydrogen evolution in reactor tests at 700 °C with the Ni/TiO_2 and $Ni–Cu/TiO_2$ catalysts prepared by impregnation and fusion method.

Source: Lázaro *et al.* (2008)

Echegoyen *et al.* (2007) reported that the catalyst calcination temperature had an effect on hydrogen yield and the structure of the carbon products. In this study, Ni-Al and Ni-Cu-Al catalysts were prepared by fusing nitric salt of nickel and copper with nitric salt of aluminium and then the mixtures were decomposed at 350 ^{o}C for 1 h and calcined at different temperatures for 8 h. Figure 12 shows the hydrogen yield obtained from methane decomposition reaction at temperature of 700 ^{o}C. It was observed that both Ni-Al and Ni-Cu-Al catalysts calcined at 600 ^{o}C presented the highest hydrogen yield. The XRD result indicated that new diffraction peaks were appeared at calcination temperatures of 800 and 1000 ^{o}C due to the formation of nickel aluminate ($NiAl_2O_4$). However, at the calcination temperature of 450 ^{o}C, nitric salts could not completely convert to nickel oxides. Moreover, copper was added into nickel catalyst to enhance the hydrogen production because copper had a strong influence on the nickel dispersion, and restrained NiO from the formation of nickel aluminate.

Copyright by Kasetsart University All rights reserved

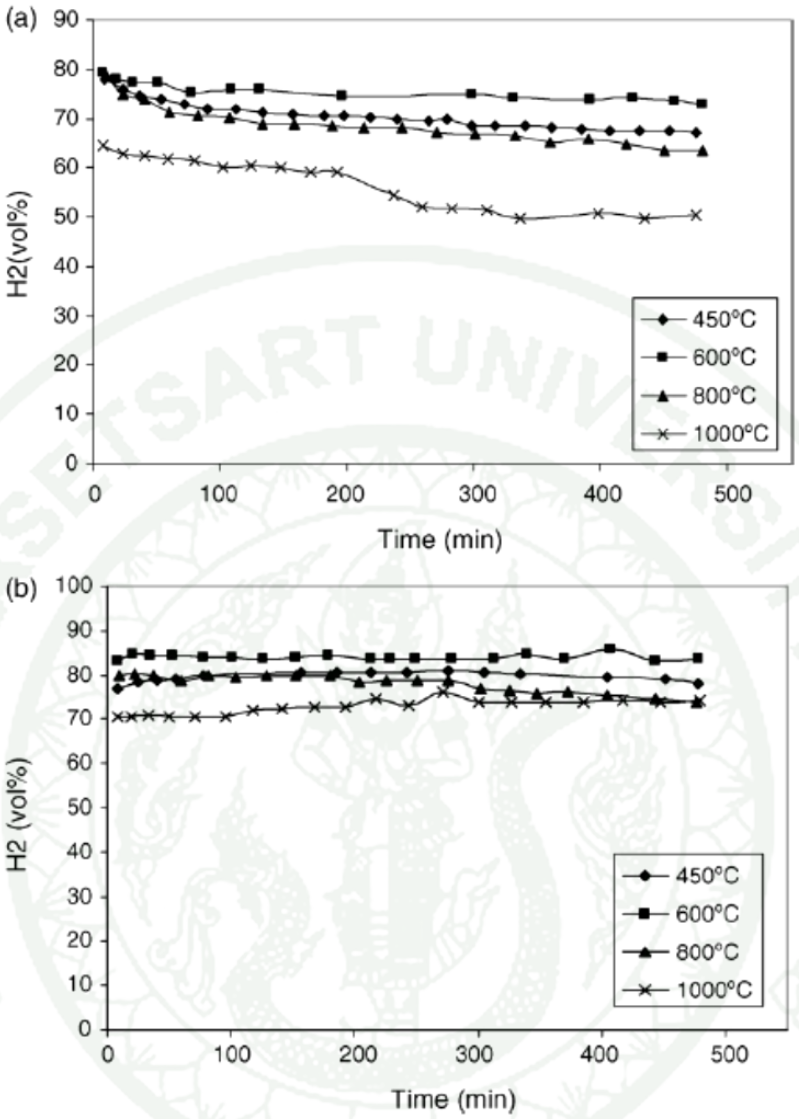

Figure 12 Effect of the calcination temperatures on the hydrogen yield: (a) Ni-Al catalyst (b) Ni-Cu-Al catalyst.

Source: Echegoyen *et al.* (2007)

Li *et al.* (2006) studied the effect of the technique of Ni/CeO_2 catalyst preparation for methane decomposition at temperature of 500 ^oC. The Impregnation, deposition-precipitation, and coprecipitation methods were used in the preparation of Ni/CeO_2 catalysts. From Figure 13, Ni/CeO_2 prepared by impregnation method gave much higher hydrogen formation rates and stable than these of Ni/CeO_2 catalysts

Copyright by Kasetsart University All rights reserved

prepared by deposition-precipitation and coprecipitation method. Moreover, carbon monoxide was also produced during methane decomposition since the lattice oxygen of ceria could react with carbons to form CO. For Ni/CeO_2 catalyst prepared by co-precipitation method, after methane decomposition reaction, Ni catalysts were covered by graphitic carbon or incorporated into the carbon nanofibers. The active surface was greatly inhibited, resulting in much lower hydrogen formation rate. In the case of Ni/CeO_2 catalysts prepared by impregnation and deposition–precipitation methods, the Ni catalysts were located on the tip of carbon nanofibers and it was still active.

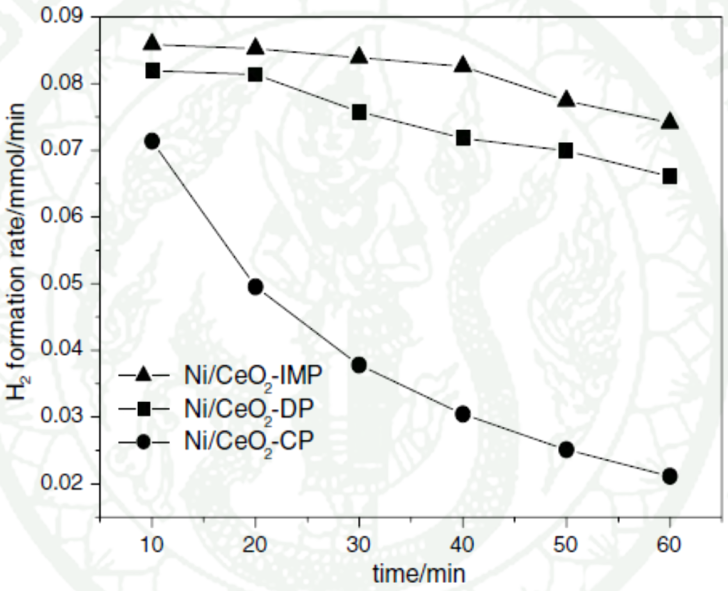

Figure 13 H_2 formation rate of methane decomposition over different preparation method of the Ni/CeO_2 catalyst at reaction temperature of 500 ^oC.

Source: Li *et al.* (2006)

4. Supported catalysts for methane cracking reaction

Apart from the metal catalysts and preparation methods, catalyst supports also played significant roles on the methane cracking reaction since they increased the distribution of the active metal catalysts, minimized catalyst sintering and extended life time of catalyst (Echegoyen *et al.,* 2007; Lua and Wang, 2012). Accordingly,

Copyright by Kasetsart University All rights reserved

various supports especially silica, titania, and alumina were frequently used in methane cracking reaction.

Takenaka *et al.* (2001) studied effects of the supports on the catalytic decomposition of methane by using 5 wt.% nickel loaded on SiO_2, TiO_2, Al_2O_3, MgO, and SiO_2·MgO. The results indicated that the activity and lifetime of catalysts in methane decomposition reaction depended on the specific surface area and pore structure of the catalysts. The silica support with no pore structure had the highest catalytic activity as well as the longest catalytic lifetime because the interaction of nickel on the silica support was less than other supports, as shown in Figure 14.

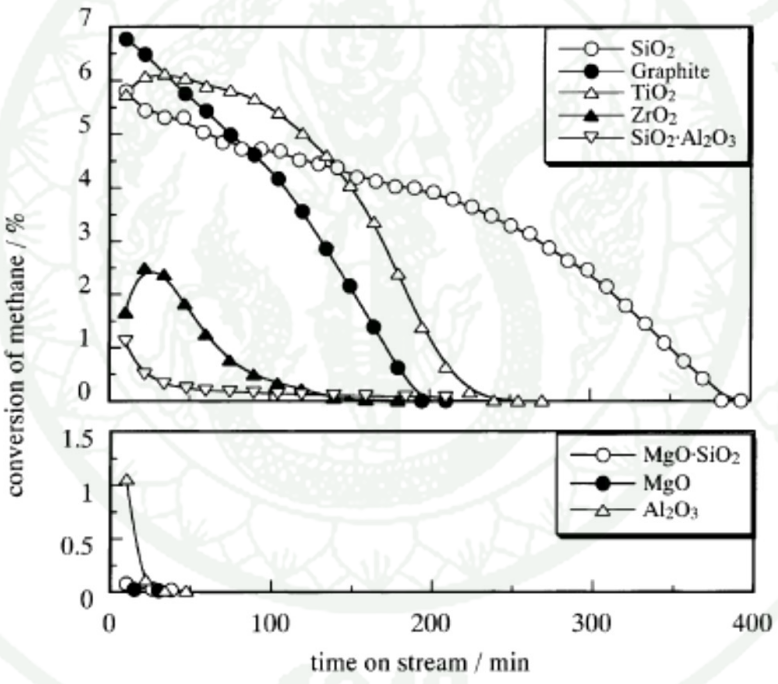

Figure 14 Methane conversion in the methane decomposition over Ni catalysts loaded on different supports at 500 ^{o}C.

Source: Takenaka *et al.* (2001)

Moreover, Takenaka and his co-workers (2001) also studied the electronic state of nickel catalyst, NiO and Ni foil by using XAS with XANES spectra in transmission mode as shown in Figure 15. The results implied that the XANES

Copyright by Kasetsart University All rights reserved

spectra of the reduced nickel catalysts with hydrogen at temperature of 550 ^{o}C, Ni/SiO_2, Ni/TiO_2, Ni/graphite and Ni/ZrO_2 were active for the methane decomposition because XANES spectra were similar to Ni foil. It indicated that Ni species in these catalysts were mainly metallic Ni. However, the XANES spectra of Ni/Al_2O_3, Ni/MgO, and $Ni/MgO{\cdot}SiO_2$ catalysts were similar to NiO, indicating the inactive form of catalysts for methane decomposition.

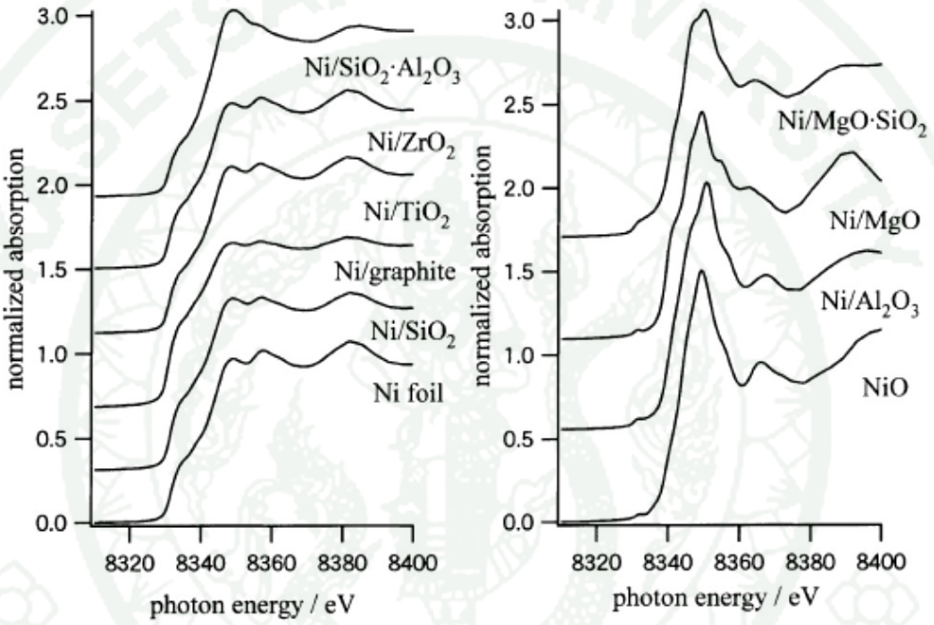

Figure 15 Ni K-edge XANES spectra of supported-Ni catalysts, NiO, and Ni foil.

Source: Takenaka *et al.* (2001)

In addition, Takenaka *et al.* (2004) loaded 20 wt.% Co on different supports including MgO, Al_2O_3, SiO_2, and TiO_2 for the formation of carbon nanofibers (CNFs) through methane decomposition. The results indicated that Co/Al_2O_3 and Co/MgO show the higher catalytic performance than Co/TiO_2 and Co/SiO_2, as shown in Figure 16. They found that the Co cluster size of Co/Al_2O_3 and Co/MgO were smaller than those of other catalysts. It should be noted that the Co cluster size of 10-30 nm could grow CNFs more easily, whereas those larger than 30 nm were inactive for methane decomposition reaction. In addition, the structure of carbon formed by methane

Copyright by Kasetsart University All rights reserved

decomposition was also depended on the reaction temperature. The multiwalled carbon nanotubes (MWCNT) were formed on Co/Al_2O_3 catalyst surface at the temperature range of 600-700 ^oC, while at 800 ^oC, helically coiled carbon nanotubes and bamboo-like carbon nanotubes were formed.

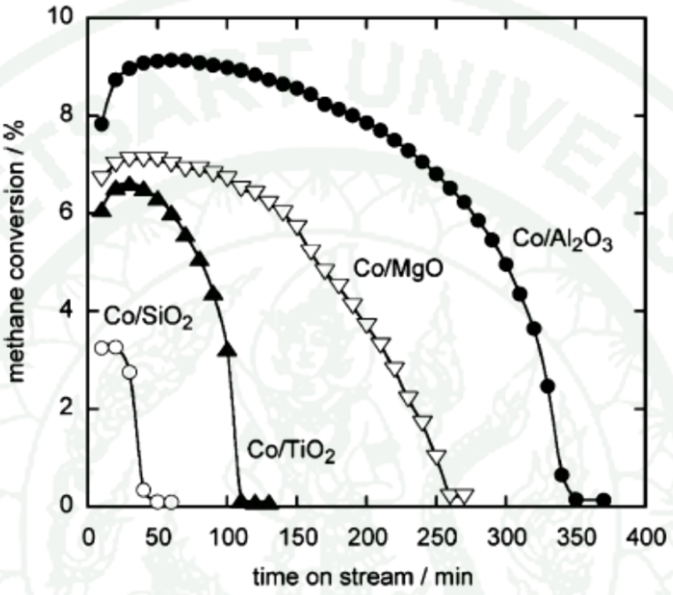

Figure 16 Methane conversion in methane decomposition at temperature of 500 ^oC over Co catalysts loaded on different supports.

Source: Takenaka *et al.* (2004)

Bonura *et al.* (2006) investigated the hydrogen production through methane decomposition on Ni supported catalysts. After the methane decomposition reaction was finished, the used catalyst was regenerated by oxygen to evaluate the activity of the regenerated catalyst. The temperature programmed catalytic reaction (TPCR) technique was applied to investigate the activity of the supported Ni catalyst, as shown in Figure 17 (a). It was observed that CH_4 conversion was increased with the reaction temperature until it reached the maximum conversion at 550 ^oC. After that, CH_4 conversion was rapidly decreased due to catalyst deactivation. Moreover, the different catalyst activities were observed. The order of the catalyst activity were CRG-F > Ni/MgO > Ni/SiO_2 > $Ni/LiAlO_2$ > Ni/ZrO_2 and the catalytic performance

Copyright by Kasetsart University All rights reserved

and regeneration activity were depended on the dispersion (Figure 17 (b)) and morphology of Ni active phase.

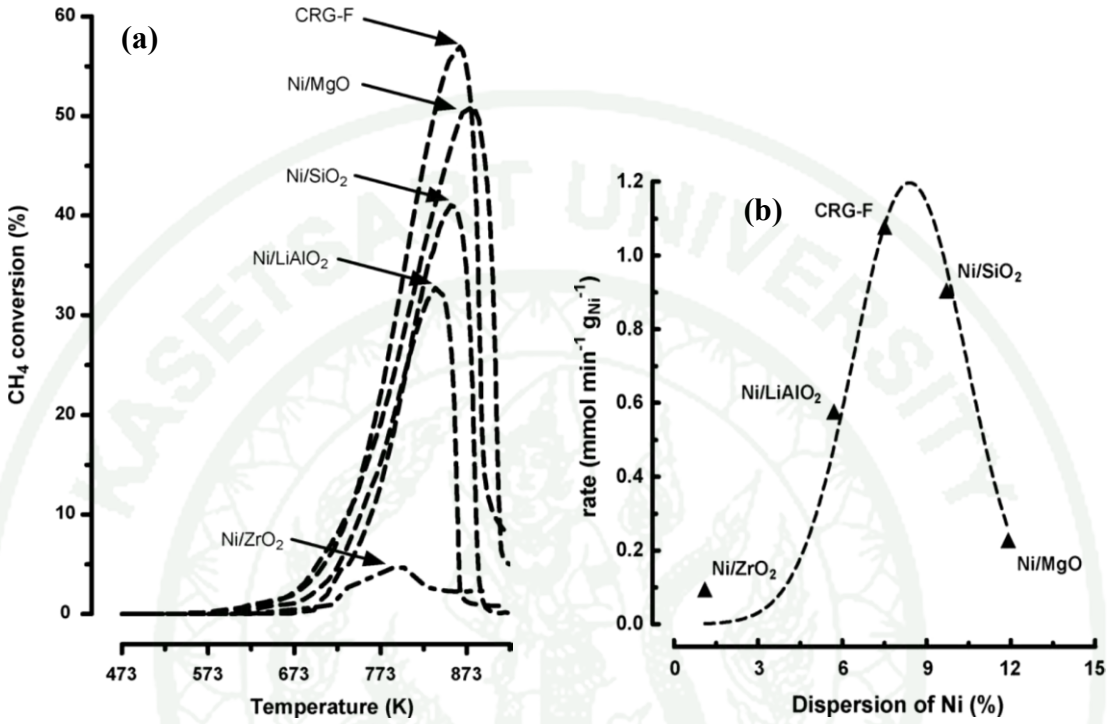

Figure 17 (a) Temperature programmed reaction of CH_4 (TPCR) over Ni supported catalysts (CRG-F is a commercial steam reforming catalyst) (b) reaction rate as a function of Ni dispersion in isothermal conditions.

Source: Bonura *et al.* (2006)

Ashok *et al.* (2007) examined the performance of 30 wt.% nickel catalyst supported on zeolites HY (surface area = 500m^2 g^{-1}, Si/Al = 2.6) and USY (surface area = 600 m^2 g^{-1}, Si/Al = 2.6, Na_2O = 4 wt.%), SiO_2 (surface area = 500 m^2 g^{-1}, pore volume = 0.75 cm^3 g^{-1}, average pore diameter = 6 nm) and SBA-15 via methane catalytic decomposition reaction at the temperature of 550 ^oC. From Figure 18, it would be seen that Ni/HY catalyst shows the better activity and longer life time. In addition, after the reaction was completed, the amount of carbon content was in the order of: HY > USY > SiO_2 > SBA-15. Among various factors as shown in Table 1,

Copyright by Kasetsart University All rights reserved

the Ni metal particle size and the acidity of the support were found to strongly influence the activity for methane decomposition reaction. Comparing zeolite supports between Ni/HY and Ni/USY, Ni loaded on HY zeolite showed the higher activity than that of USY zeolite support due to the presence of 4% Na_2O.

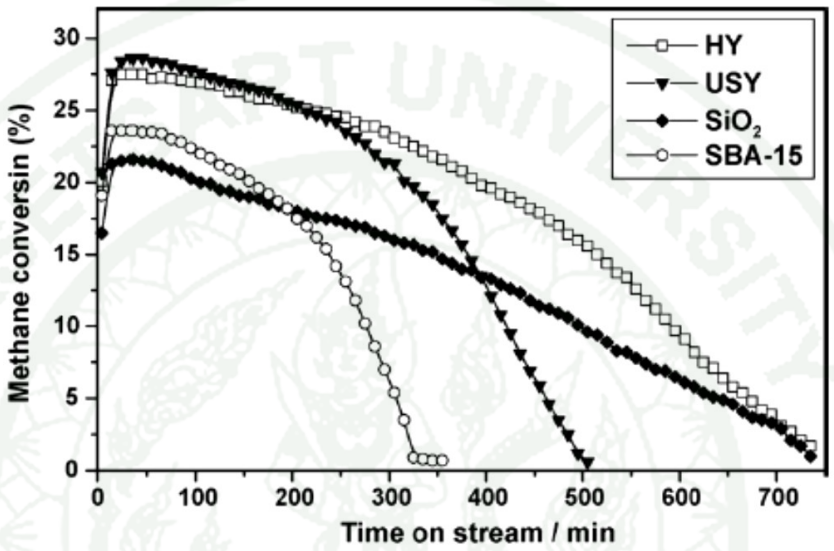

Figure 18 Methane conversion during methane decomposition over 30 wt.% Ni supported catalysts at 550 ^{o}C.

Source: Ashok *et al.* (2007)

Table 1 Summary of the experiments conducted

Catalyst	Run time (min)	Ni crystallite size	H_2 yield (mol mol^{-1})	Acidic strength E_i (mV)	H_2 uptakes (mmol g^{-1})[a]
HY	720	18	955	173	4.6
USY	515	20	712	110	4.5
SiO2	720	21	677	158	5.0
SBA-15	400	24	400	255	5.6

[a] H_2 uptakes were calculated from TPR profiles.

Source: Ashok *et al.* (2007)

Copyright by Kasetsart University All rights reserved

Guevara *et al.* (2010) synthesized mesoporous Ce-MCM-41 supports and loaded with Ni metal, and used as the catalyst in methane decomposition reaction. The results show that Ni/Ce-MCM-41 catalysts were very stable and the methane conversion could be remained almost unchanged during 1400 min time on stream at the reaction temperatures of 540, 560, and 580 ^{o}C (methane conversion ~ 60-75%). The long life time and stability of these catalysts were obtained because Ni particles were located on the tip of carbon nanofibers or nanotubes in the used catalysts, and exposed the clean surface (remaining active). Moreover, the basic or redox promoters (Ce) added during synthesis Ce-MCM-41 could eliminate the carbon formation on the surface of the catalyst.

Amin *et al.* (2012) studied the effect of alumina structure of Ni/γ-Al_2O_3 (porous alumina) and Ni/α-Al_2O_3 (nonporous alumina) on the catalytic methane cracking/regeneration cycles. Methane cracking was studied through the thermogravimetric analysis to observe the weight changes from carbon formation. Besides, the effects of methane and hydrogen partial pressure, temperature, and flow rate on methane cracking reaction were also investigated. The results show that the methane partial pressure had less effect on the amount of carbon formed on the surface of catalysts at all temperatures. The initial cracking rate was decreased with the increase of hydrogen partial pressure at all temperatures. From the results, the fresh nonporous catalyst had the higher activity than the fresh porous catalyst, while after the regeneration the nonporous catalyst had lower activity than the porous catalyst. Moreover, the carbon filaments were occurred only on the surface of the porous catalyst after methane cracking reaction.

From the results mentioned above, the types of supported catalyst had the significant effect on the catalytic performance of methane cracking reaction. This section described the basic information of support preparation, focusing especially on the sol-gel method as in this research the monomodal and bimodal porous silica supports were synthesized by the sol-gel method.

Copyright by Kasetsart University. All rights reserved

The sol-gel method was a preferable technique to synthesize the porous materials. A transformation of liquid sol (colloid) to a solid gel phase occurred. In this technique, the colloid was prepared by using water and inorganic compounds (low molecular weight alkoxide) as precursors. There are wide varieties of low molecular weight alkoxides, such as tetraethoxysilane ($Si(OC_2H_5)$: TEOS), aluminum isopropoxide ($C_9H_{21}AlO_3$: AIP) or tetramethoxysilane (TMOS), which could be used as the silica and alumina precursors (Iler, 1979). The alkoxide would be reacted with water (hydrolysis reaction) to form the silanol groups (≡Si-OH), where either acid or base was used as the catalyst in this process, as shown in Equation (3). The silanol groups could link together in a condensation reaction (water condensation or alcohol condensation) as shown in Equations (4) and (5).

Hydrolysis reaction

$$\equiv Si - OR + H_2O \longleftrightarrow \equiv Si - OH + ROH \quad (3)$$

Water condensation

$$\equiv Si - OH + HO - Si \equiv \longleftrightarrow Si - O - Si \equiv + H_2O \quad (4)$$

Alcohol condensation

$$\equiv Si - OH + RO - Si \equiv \longleftrightarrow Si - O - Si \equiv + ROH \quad (5)$$

In the condensation step, a larger molecule could be produced by polymerization, where porous silica was formed in this step. The polymerization consisted of three stages: (1) polymerization of monomer ($Si(OH)_4$) to form particles, (2) growth of particles, and (3) linkage of particles together into chains and then networks extending throughout the liquid medium, and thickening to a gel. The schematic diagram of polymerization behavior of silica is shown in Figure 19.

Copyright by Kasetsart University All rights reserved

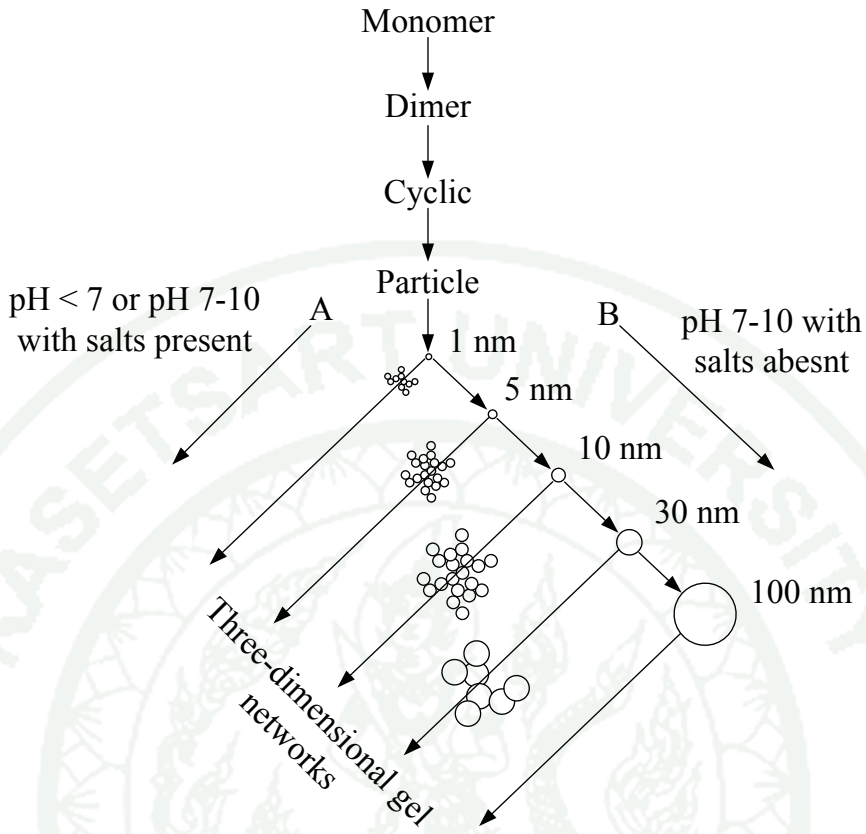

Figure 19 Polymerization behavior of silica: In acid solution or in presence of flocculating salts (A), particles aggregate into three-dimensional networks and form gels; In basic solution (B) particles in sol grow in size with decrease in numbers.

Source: Iler (1979)

The bimodal (meso-macro) porous materials could be synthesized by sol-gel technique with the addition of the template to create the phase separation in the gel product. Takahashi *et al.* (2007) synthesized Ni/SiO_2 catalysts with a bimodal pore structure by sol-gel method. Polyethyleneoxide (PEO) was used in the catalyst synthesis to induce the phase separation. The size of macropore could be controlled by changing the solution composition and aging temperature. Moreover, urea was added during the sol-gel method resulting in higher pH value of gel products. The increasing on pH in gel led to the ripening of silica gel network and homogeneous

Copyright by Kasetsart University All rights reserved

deposition of nickel hydroxide. The result shows that these catalysts have high dispersion of Ni.

Witoon *et al.* (2008) synthesized the bimodal porous silica (BPS) by adding chitosan (template) into sodium silicate solution. The pH of mixture was adjusted to increase the size of macropore. Figure 20 shows the TEM images of bimodal meso-macroporous silica with adjusting pH during the synthesis process. It could be clearly seen that the pore size of BPS was increased with increasing the pH of mixture.

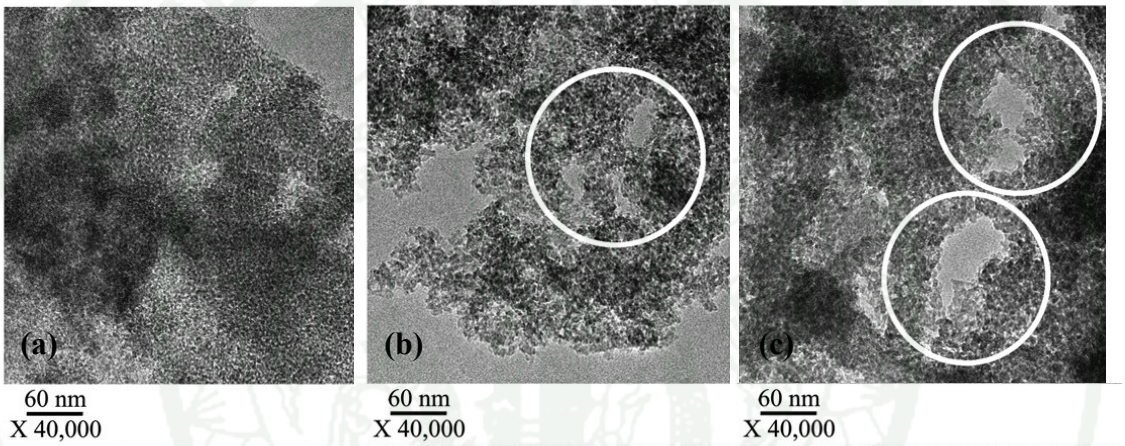

Figure 20 TEM image of meso-macro porous silica with adjusting pH (a) pH = 2 and (b) pH = 3 (c) pH = 5.

Source: Witoon *et al.* (2008)

As mentioned above, the deactivation of nickel supported catalysts occurred from covering the nickel clusters with carbon or the space limitations. Therefore, bimodal pore structures with mesopore and macropore could possibly lessen the catalyst deactivation. In this research, two bimodal porous silica supports with mesopore structure and meso-macropore structure were synthesized following Kiatphuengporn *et al.* (2014) and Witoon *et al.* (2008), respectively. Two monomodal porous silica supports were also synthesized to compare the effect of bimodal porous silica supports. The relationships between catalytic performance and characterization of the fresh and used catalysts were discussed based on the results

Copyright by Kasetsart University All rights reserved

obtained from N_2-sorption, XRD, TPR, XAS, SEM, TGA-DTA, and Raman spectroscopy.

Copyright by Kasetsart University All rights reserved

MATERAILS AND METHODS

The effect of bimodal porous silica support on stability of nickel catalysts was investigated through methane cracking reaction. There are two main parts in this section consisting of (1) catalyst support preparation (2) the synthesis of carbon filament and H_2 via methane cracking reaction. The bimodal and monomodal porous silica supports were synthesized by sol-gel method. The details of equipments, support and catalyst syntheses were shown as follows

Synthesis of porous silica supports

1. Equipments of Bimodal and Monomodal Porous Silica Synthesis

1.1. Magnetic hot plate and stirrer (Schott, SLR)

1.2. Furnace (Carbolite, ELF10/6)

1.3. Digital balance (Metler Toledo, AT 400)

1.4. Hot air oven (Binder,ED53)

1.5. Autoclave (made by order)

2. Materials of Bimodal and Monomodal Porous Silica Synthesis

2.1 Sodium silicate (Na_2SiO_3: 32 wt% SiO_2, PQ Chemical)

2.2 Chitosan (Eland Corporation, 90.0 % deacetylation)

2.3 Pluronic P123 ($PEO_{20}PPO_{70}PEO_{20}$: Aldrich; Product code No. 435-465)

2.4 Cethyltrimethyl ammonium bromide ($C_{16}H_{33}N$ $(CH_3)_3$-Br, CTAB: AJAX, No. A147)

2.5 Tetraethyl orthosilicate (TEOS: 99% SiO_2, ALDRICH)

2.6 Ammonia solution (NH_3: 28% purity, QRëC)

2.7 Sodium hydroxide (NaOH: Merck; Purity, 99.0 %)

2.8 Hydrochloric acid (HCl: J.T. Baker; Purity, 36.5 -38.0 wt. %)

2.9 Acetic acid, CH_3COOH (CH_3COOH: BDH; Purity, 100%)

2.10Distilled water

Copyright by Kasetsart University All rights reserved

3. Bimodal and Monomodal Porous Silica Synthesis

In order to synthesize bimodal and monomodal porous silica, sodium silicate and TEOS were used as the silica source for bimodal and monomodal porous silica synthesis. The porous silica supports were synthesized via sol-gel method. The preparation of bimodal and monomodal porous silica products were shown as follows:

3.1 Bimodal porous silica syntheses

In this research, methane cracking reaction was performed over the bimodal porous silica supports to study the effect of pore size and pore characteristic on deactivation of catalyst.

3.1.1 Bimodal porous silica-5 synthesis (BPS-5)

The porous structures of bimodal porous silica-5 were the combination of mesopore and macropore structures, which formed between each of silica nanoparticle, resulting in the wormhole pore structure created. The chitosan was used as the templates for creating macropore after template was removed by calcinations.

A chitosan solution can be prepared by dissolved 0.4 g of chitosan in 100 ml of 1% v/v acetic acid in deionized water at temperature of 40 ^{o}C. Then, sodium silicate solution (based on the 1 g of silica) was primarily diluted with 10 ml of deionized water and slowly added to the chitosan solution with vigorous stirring. The pH values of solution were adjusted to 5 with 2 M HCl and 2 M NaOH solutions. After that, the hydrolysis-condensation reaction was carried out at 40^{o}C for 3 h, and then the obtained gel was aged in the Teflon-lined autoclave at 100 ^{o}C for 24 h. The solid products were filtrated, washed several times with distilled water, dried at 100 ^{o}C for 24 h and calcined at 550 ^{o}C for 5 h with the heating rate of 2 ^{o}C/min.

Copyright by Kasetsart University All rights reserved

3.1.2 Mesoporous silica MCM-41 synthesis

The porous structures of bimodal mesoporous silica MCM-41 were the combination of mesopore structures, which has the pore diameter below 50 nm. The CTAB was used as the templates for creating straight pore (small pore) after template was removed by calcinations. Moreover, the larger interconnected wormhole structure was formed between aggregation of each silica nanocluster.

A cetyl trimethylammonium bromide (CTAB) of 1.21 g was dissolved in 48.12 ml of deionized water at room temperature. Then, tetraethyl orthosilicate (TEOS) of 3.708 ml was slowly dropped into CTAB solution and then NH_3 solution of 0.5 ml was added into the solution under vigorous stirring. After that, the hydrolysis-condensation reaction was carried out at 40 ^{o}C for 24 h, and then the obtained gel was aged in Teflon-lined autoclave at 100 ^{o}C for 24 h. The solid product was filtrated, washed several times with deionized water, dried at 100 ^{o}C for 24 h and calcined at 550 ^{o}C for 4 h with the heating rate of 5 ^{o}C/min.

3.2 Monomodal porous silica systhesis

The monomodal porous silica products, xerogel with pH of solution at 5 and SBA-15, were synthesized in order to compare the results with those of the bimodal porous silica products.

3.2.1 Monomodal porous silica (Xerogel-5) synthesis

The mesopore structure of Xerogel-5 was created by aggregation of silica nanoparticles, which wormhole structure formed.

Sodium silicate solution (based on 1 g of silica) was primarily diluted with 10 ml of deionized water and slowly dropped into 100 ml of 1% v/v acetic acid in deionized water under vigorous stirring. The pH values of solution were adjusted to 5.

Copyright by Kasetsart University All rights reserved

After that, the hydrolysis-condensation reaction was carried out at 40 ^{o}C for 3 h, and then the obtained gel was aged in the Teflon-lined autoclave at 100 ^{o}C for 24 h. The solid products were filtrated, washed several times with distilled water, dried at 100 ^{o}C for 24 h and calcined in air at 550 ^{o}C for 5 h at the heating rate of 5 ^{o}C/min.

3.2.2 Mesoporous silica SBA-15 synthesis

The mesopore structure of SBA-15 was created by Pluronic P123. It were used as the templates after calcination, the straight pores created by template removal were obtained.

Pluronic P123 of 0.845 g was dissolved in deionized water of 60 ml for overnight. Then, sodium silicate was slowly dropped into Pluronic P123 solution that was being stirred at 40 ^{o}C and then 5.4 ml HCl was added into the solution. After that, the hydrolysis-condensation reaction was carried out at 40 ^{o}C for 24 h and then the resultant solution was aged in Teflon-lined autoclave at 100 ^{o}C for 24 h. The solid product was filtrated, washed several times with deionized water, dried at 100 ^{o}C for 24 h and calcined in air at 550 ^{o}C for 6 h at the heating rate of 2 ^{o}C/min.

4. Characterization of bimodal and monomodal porous silica

4.1 N_2-sorption measurement

BET surface area, adsorption-desorption isotherms, pore size distribution, and pore volume of bimodal and monomodal porous silica products were analyzed by using N_2-sorption equipment of Quantachrome Corporation (Model: Autosorb1). Prior to each measurement, samples were degassed at 200 ^{o}C under vacuum and followed by flowing helium gas to remove adsorbed water and other volatile matters from the surface of solid samples. The measurement was done at high vacuum level (10^{-4} torr) at the temperature of liquid N_2 (-196 ^{o}C) using the total N_2 adsorption/desorption points of 55 points.

Copyright by Kasetsart University All rights reserved

4.2 Small angle X-ray scattering (SAXS)

The diffractograms of silica supports were investigated by X-ray diffraction (XRD: JEOL JDX-3530 and Philips X-Pert) using Cu Ka radiation at low angle in the range of 0-10 ^{o}.

Synthesis of Nickel on Silica Catalyst

1. Equipments of Nickel on Silica Catalyst Synthesis

1.1 Magnetic hot plate and stirrer (Schott, SLR)
1.2 Furnace (Carbolite, ELF10/6)
1.3 Digital balance (Metler Toledo, AT 400)
1.4 Microwave (MS2127CW, LG)

2. Materials of Nickel on Silica Catalyst Synthesis

2.1 Nickel nitrate ($Ni(NO_3)_2$•$6H_2O$: 97.0% purity, Unilab)
2.2 Distilled water
2.3 Bimodal and monomodal porous silica supports

3. Loading of Ni metal onto bimodal and monomodal porous silica supports

Nickel metal of 5 wt.% was loaded onto 0.5 g of monomodal and bimodal porous silica supports via incipient wetness impregnation method. The solution of metal precursor was prepared by dissolving certain amount of nickel nitrate ($Ni(NO_3)_2 \cdot 6H_2O$) in a required amount of deionized water under stirring. The obtained products were dried with using microwave at 800 watt for 1 minute and calcined in air at 550 °C for 5 h. The nickel loaded on monomodal and bimodal porous silica catalysts were obtained and denoted as Ni/BPS-5, Ni/MCM-14, Ni/Xerogel-5 and Ni/SBA-15.

Copyright by Kasetsart University All rights reserved

4. Catalyst characterization

4.1 Surface area, pore size distribution and pore volume

The specific surface area, pore volume, BJH pore diameter, and pore size distribution of the catalysts were determined by N_2 physisorption using a Quantachrome Autosorb-1C instrument at -196 ^{o}C. Prior to each measurement, samples were degassed at 200 ^{o}C for 12 h. The pore size distribution and pore volume were determined by BJH method and the specific surface area was estimated by BET method.

4.2 X-ray powder diffraction (XRD)

X-ray powder diffraction measurement was performed at room temperature using a Phillips powder diffractometer with monochromatized Cu-Kα radiation. Nickel oxide phases were detected by comparing the diffraction patterns with those of the standard powder XRD file compiled by the joint committee on powder diffraction standards (JCPDS) published by the International Center for Diffraction Data. The NiO crystallite diameters were calculated by using Scherrer equation (as shown below) from the most intense NiO peak at 2θ of 43.35.

$$d = \frac{0.9\lambda}{B \cos \theta} \times \frac{180^{o}}{\pi}$$

where d is the mean crystallite diameter

λ is the X-ray wave length (1.54 A°)

B is the full width half maximum (FWHM) of the NiO diffraction peak.

4.3 Temperature programmed reduction (TPR)

The reduction temperature of catalysts were determined by temperature programmed reduction (TPR) using a continuous-flow tube reactor (Inconel-600,

Copyright by Kasetsart University All rights reserved

O.D. 3/8") in the temperature range of 25-900 ^{o}C. The H_2 mixed with Ar (9.6% H_2 balanced with Ar) was fed into reactor and H_2 consumption was reported by using Shimadzu gas chromatograph (GC-2014) equipped with a thermal conductivity detector (TCD).

4.4 X-ray absorption spectroscopy (XAS)

X-ray absorption measurements were carried out using the beam line BL-8 at the Synchrotron Light Research Institute (Public Organization), with energy range of 1.25 keV to 10 keV. The electronic properties of catalysts especially their electronic stages of Ni element (Ni K-edge) were analyzed by using XAS with XANES spectra in transmission mode between 8300 and 8430 eV.

4.5 Scanning electron microscopy (SEM)

Surface morphology of catalysts after methane cracking reaction was examined by using JEOL JSM6301-F. The powder sample was attached on a carbon tape over alumina specimen mount, and coated with gold (Au) using a sputtering technique.

4.6 Thermogravimetric analysis (TGA-DTA)

The amount and temperature of carbon degradation of carbon deposited on catalyst surface were determined by using TA instrument SDT2960 Simultaneous TGA-DTA Universal 2000. In this analysis, the sample was heated from room temperature to 1000 ^{o}C at heating rate 5^{o}C/min in air.

4.7 Raman spectroscopy

The crystallinity, structure and order of carbon deposited on catalyst surface after methane cracking reaction were analyzed by using Raman spectroscopy (NTEGRA spectra, NT-MDT).

Copyright by Kasetsart University All rights reserved

Synthesis of H_2 and Carbon Filaments via Methane Cracking Reaction

1. Equipments of Methane Cracking Reaction

1.1. Pressure regulator

1.2. Mass flow controller (8300 Series, KOFLOC)

1.3. Mass flow controller (GFC117, Aalborg)

1.4. Thermocouple (K-type)

1.5. Inconel-600 tube reactor O.D. 3/8" (Alloy 600, Lotus Metal (Thailand) Co., Ltd.)

1.6. Tube furnace (CFW 1300, Carbolite)

1.7. Temperature indicator (RI, Shino)

1.8. Bubble flow meter

1.9. Gas chromatograph equipped with thermal conductivity detector (TCD) and chromatopac data processor (GC-2014, Shimadzu)

1.10. Gas-tight syringes (1002LTN Gastight Syringe, Hamilton and A-2 type Gas tight Syring, PS)

2. Material for Methane Cracking Reaction

2.1 Reactant gases

2.1.1 Methane (CH_4: 99.99% purity, TIG)

2.1.2 Nitrogen (N_2: 99.99% purity, TIG)

2.1.3 Hydrogen (H_2: 99.99% purity, TIG)

2.2 Standard gases

Mixture of 25% carbon dioxide (CO_2), 25% carbon monoxide (CO), 25% methane (CH_4) and 25% hydrogen (H_2).

2.3 Quartz wool as the catalyst bed support (Alltech)

Copyright by Kasetsart University All rights reserved

3. Performance Testing of Methane Cracking Reaction

The experimental unit for the methane cracking reaction is shown in Figure 21. It consists of a feed flow measuring and controlling system, a furnace equipped with inconel-600 tube reactor and a sampling system. The catalytic reaction testing unit was designed to operate under high temperature and atmospheric pressure conditions. The details of particular system are explained below.

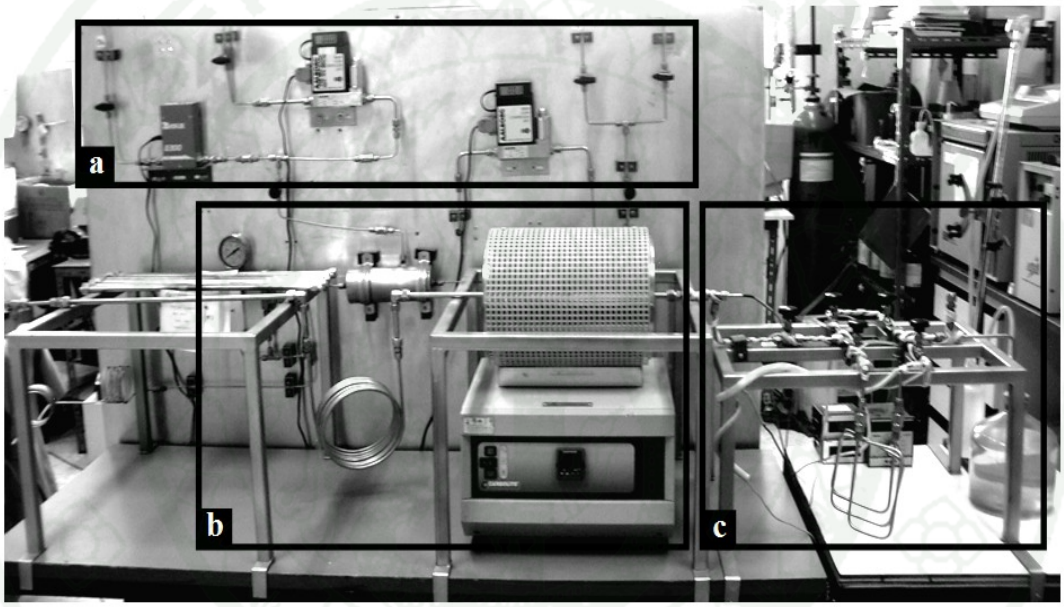

Figure 21 Catalytic reaction testing unit: (a) a feed flow measuring and controlling system, (b) a furnace-equipped inconel-600 tube reactor and (c) a sampling system.

3.1 The feed flow measuring and controlling system

In this system, mass flow controllers were used to finely control and indicate the flow rate of feed gases including methane, nitrogen and hydrogen. Methane diluted with nitrogen was used as a reactant gas and hydrogen was used for the reduction of catalyst. In order to monitor the system leakage, nitrogen gas was also applied. Flow rates of methane and hydrogen were measured and controlled by

Copyright by Kasetsart University All rights reserved

KOFLOC mass flow controller (Figure 22a) and Aalborg mass flow controller (Figure 22b) was use to control the flow rate of nitrogen.

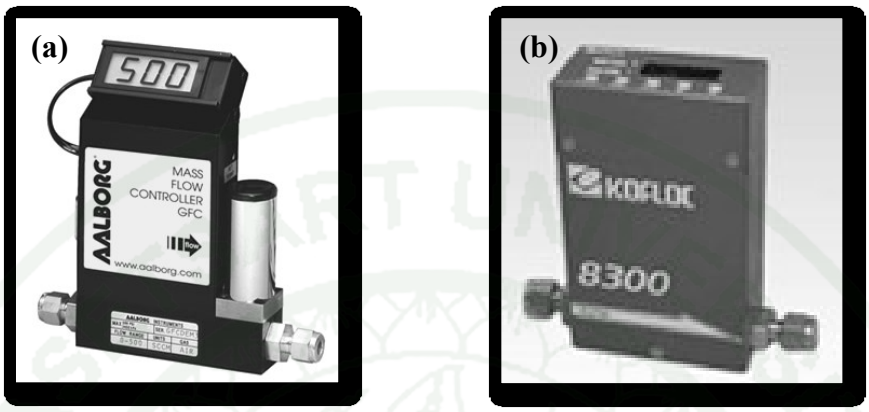

Figure 22 Mass flow controller: (a) Aalborg GFC thermal mass flow controller and (b) KOFLOC mass flow controller and mass flow meter with indicator.

3.2 The packed bed reactor

The inconel tube of 3/8" O.D. and 40 cm length was used as the fixed-bed reactor. At the stage of reduction and methane cracking reaction, the inconel-600 tube was heated with an electric heater (Figure 23) controlled by the temperature controller. The K-type thermocouple connected to a temperature controller unit was inserted inside the inconel-600 tube in order to measure and control the temperature of the catalyst bed. The catalyst powder was packed in the isothermal zone of tube reactor between quartz wool layers as the scheme shown in Figure 24.

Copyright by Kasetsart University All rights reserved

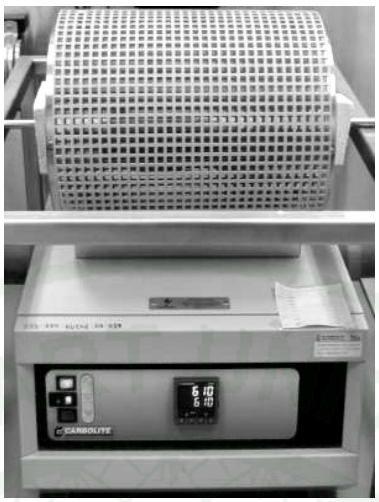

Figure 23 The reactor of methane cracking reaction equipped with the electric heater (Carbolite tube furnace).

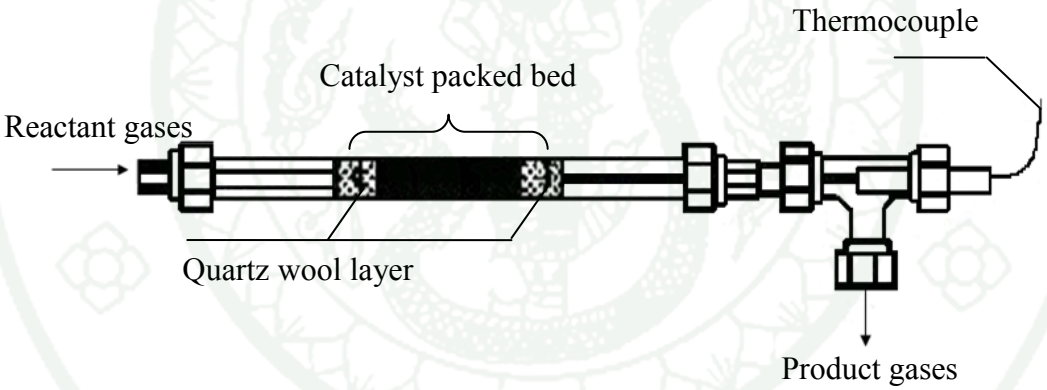

Figure 24 Schematic setup of the stage of methane cracking reaction reactor.

3.3 Gas analysis unit

The gas chromatograph was applied to analyze the reactant and product gases. Gas analysis unit (Figure 25) consists of Shimadzu gas chromatograph and chromatopac data processor (GC-2014) equipped with thermal conductivity detector (TCD). A Unibead-C packed column was used to analyze CH_4, N_2 and H_2 by using argon (99.99% purity) was used as the carrier gas.

Copyright by Kasetsart University All rights reserved

Figure 25 Shimadzu gas chromatograph (GC-2014) equipped with thermal conductivity detector (TCD) and chromatopac data processor.

The conditions for CH_4, N_2 and H_2 analysis were:

- Initial carrier gas (Ar) flow rate	25	ml/min
- Final carrier gas (Ar) flow rate	25	ml/min
- Injector temperature	150	^oC
- Initial column temperature	150	^oC
- Final column temperature	150	^oC
- Detector temperature (Pre)	150	^oC
- Detector temperature	150	^oC
- Current	60	mA

3.4 Test for methane cracking reaction

Before testing the catalytic performance, 0.1 g of nickel on silica catalyst was thoroughly mixed with 1.5 g of sand, in order to avoid the effect of poor heat transfer during methane cracking experiment. The catalyst with sand was packed in inconel-600 tube reactor. Prior to each experiment, the catalyst was reduced by using H_2 at atmospheric pressure and temperature of 600 °C for 3 h with the flow rate of 60 ml/min (NTP) and then flushed with nitrogen gas. After pretreatment procedure, the catalyst was ready for the catalytic performance test.

Copyright by Kasetsart University All rights reserved

During the reaction, CH_4 was decomposed to hydrogen and carbon filaments, deposited on surface of catalysts at atmospheric pressure and temperature of 500, 550, 600 and 650 °C with 20% CH_4 in N_2 balanced at total gas flow rate of 100 ml/min.

Copyright by Kasetsart University All rights reserved

RESULTS AND DISCUSSION

In this research, bimodal and monomodal porous silica with different pore sizes and pore structures were used as nickel metal supports in order to investigate the effect of pore characteristics on the deactivation of catalysts in methane cracking reaction. The nickel catalysts were prepared by using incipient wetness impregnation base on 5 wt.% nickel loading. The catalytic performances on methane cracking reaction were tested under atmospheric pressure, reaction temperatures of 500-650 °C and total flow rate of 100 ml/min with volume ratio of CH_4:N_2 equal to 1:4. The effect of active nickel supported over bimodal porous silica catalysts denoted as Ni/BPS-5 and Ni/MCM-41, and monomodal catalysts denoted as Ni/Xerogel-5 and Ni/SBA-15 were clarified and reported.

1. Physical and Chemical Properties of Catalysts

In this part, the adsorption-desorption isotherms, pore size distribution, BET surface area, total pore volume, average pore diameter of porous silica supports and catalysts were discussed. Moreover, types of nickel species, average NiO crystallite size and reduction temperature of nickel metal catalyst were investigated.

N_2-sorption technique was used to investigate the physical properties of bimodal and monomodal porous silica supports, and nickel supported on bimodal and monomodal porous silica supports. Figures 26 (A) and (B) show adsorption-desorption isotherms of porous silica supports and nickel catalysts, respectively. For MCM-41, Xerogel-5, and SBA-15 (Figure 26(A)), type IV isotherms with hysteresis loop indicating the existence of mesopore structure were observed. It found that capillary condensation steps of MCM-41 shifted to higher relative pressure than Xerogel-5 and SBA-15 because MCM-41 has bimodal pore size and its average pore size was larger than those of Xerogel-5 and SBA-15. In the case of BPS-5, the composite isotherm between type II and type IV was observed as shown in Figure 26(A), indicating that BPS-5 consisted of mesopore and macropore structures.

Copyright by Kasetsart University All rights reserved

Moreover, the result of adsorption-desorption isotherms of nickel loaded on bimodal and monomodal porous silica supports (Figure 26(B)) exhibited the same trends as unloaded porous silica supports. However, the volumes of gas adsorbed were clearly decreased when compared to those of unloaded porous silica supports due to the fact that the pores of porous silica supports were partially blocked by nickel oxide clusters.

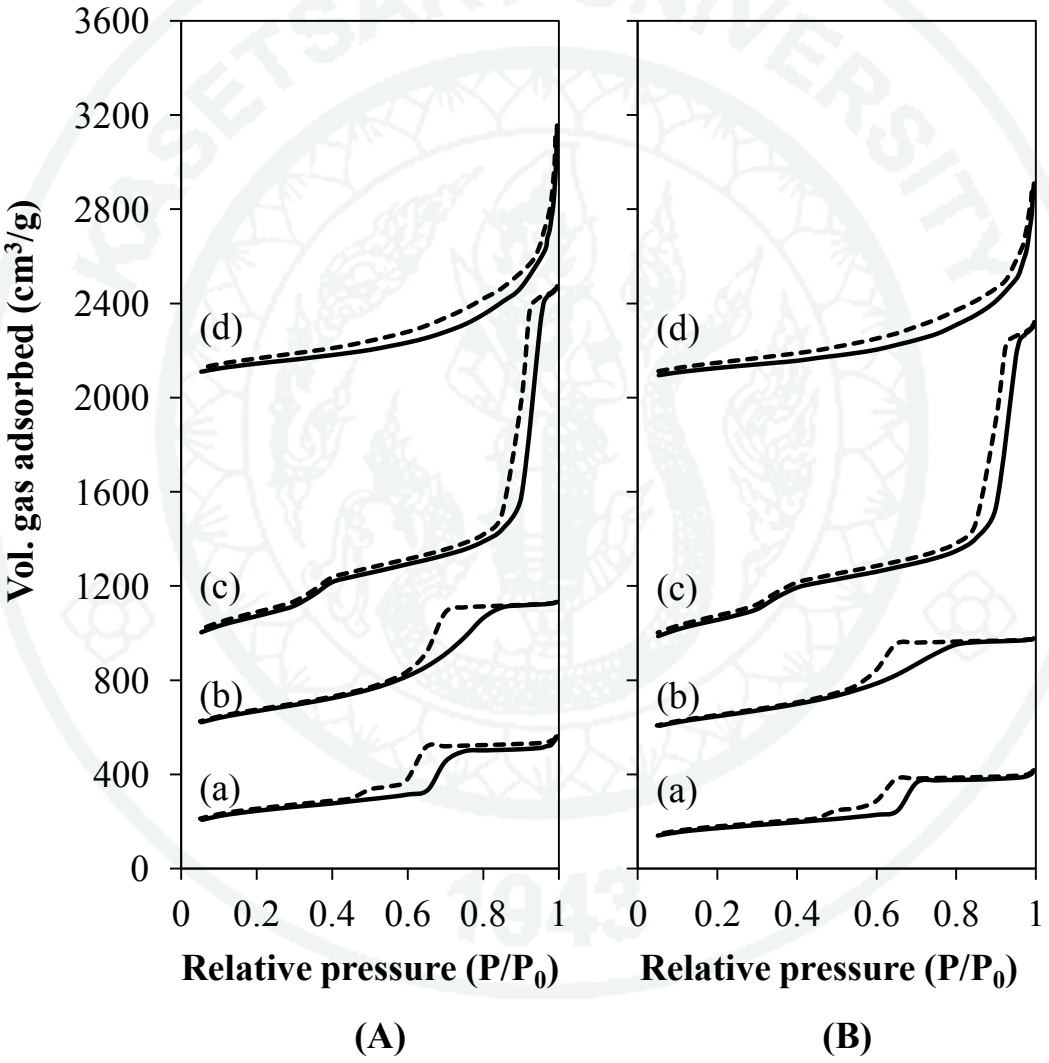

Figure 26 Adsorption-desorption isotherm of (A) porous silica supports (a) SBA-15 (b) Xerogel-5 (c) MCM-41 and (d) BPS-5 and (B) nickel loaded on porous silica supports (a) Ni/SBA-15 (b) Ni/Xerogel-5 (c) Ni/MCM-41 and (d) Ni/BPS-5.

Copyright by Kasetsart University All rights reserved

The pore size distribution of porous silica supports and nickel loaded on porous silica supports were shown in Figures 27(A) and (B), respectively. SBA-15 and Xerogel-5 exhibited a single peak (Figure 27(A)), indicating the existence of monomodal pore structure with pore diameters of both 6.5 nm, as shown in Table 2. Moreover, MCM-41 and BPS-5 supports show two main peaks at 2.7 and 24 nm, and 6-100 and 200 nm, respectively as shown in Figure 27(A). This result clearly indicated that MCM-41 and BPS-5 supports were bimodal porous silica supports. In addition, Xerogel-5, SBA-15, and MCM-41 show the sharp and narrow pore size distributions, indicating that the uniform pore sizes and structures were created. On the other hand, BPS-5 exhibited broader pore size distribution due to the nature of chitosan template at relatively high pH value.

Based on pore structures, the porous silica supports used in this study could be classified into 2 types including straight-pore and sinusoidal-pore, of with SBA-15 and MCM-41 were the straight-pore supports, while Xerogel-5 and BPS-5 were the sinusoidal-pore supports. In the case of BPS-5 and Xerogel-5, the pore structure was formed by an aggregation of silica nanoparticles, resulting in the interconnected wormhole structure. However, in the case of MCM-41 and SBA-15, CTAB and Pluronic P123 were used as the 2-D hexagonal pore templates, respectively. After calcination, the straight pores created by template removal were obtained. In addition, with MCM-41, the silica nanoclusters obtained during hydrolysis-condensation process were consecutively aggregated and relatively larger interconnected wormhole structure was also formed. Pore size distributions of nickel loaded on bimodal porous and monomodal silica supports are shown in Figure 27(B). The similar results as unloaded catalysts were observed.

The physical properties such as BET surface area, BJH pore diameter, total pore volume of these supports and the nickel-loaded catalysts are listed in Table 2. Comparing between Xerogel-5 and BPS-5, it was observed that BET surface area of BPS-5 was lower than that of Xerogel-5. This could be attributed to the fact that after calcinations the large pore of BPS-5 was created by chitosan template removal, leading to the decrease of BET surface area. Moreover, BET surface area of MCM-41

Copyright by Kasetsart University All rights reserved

was the highest than other silica supports because the smaller and uniform mesopore (2.7 nm) of MCM-41 supports could enhance BET surface area. However, it can be clearly seen that BET surface area and pore volume of the supports after nickel metal loading were significantly decreased because the nickel particles could partially block the pores of porous silica supports.

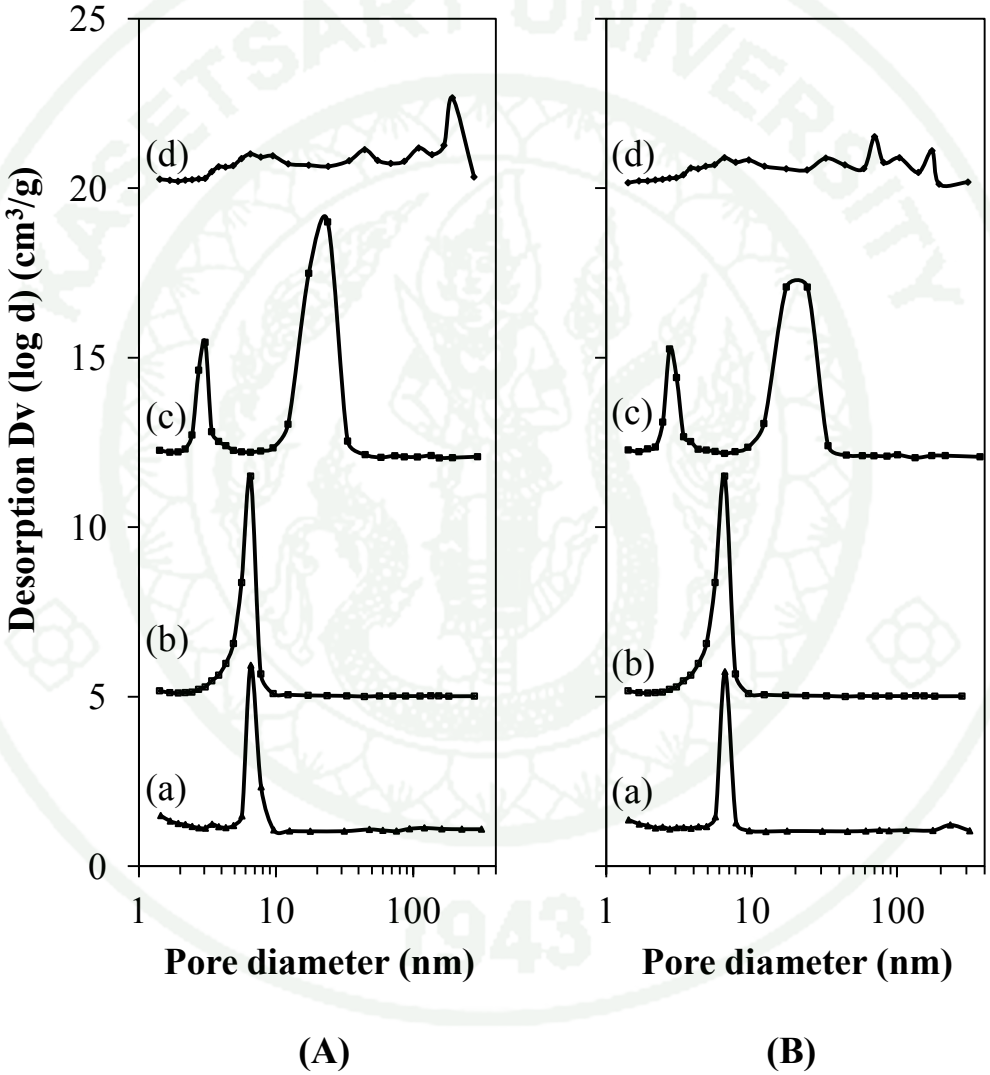

Figure 27 Pore size distribution of (A) porous silica supports: (a) SBA-15 (b) Xerogel-5 (c) MCM-41 and (d) BPS-5, and (B) nickel loaded on porous silica supports: (a) Ni/SBA-15 (b) Ni/Xerogel-5 (c) Ni/MCM-41 and (d) Ni/BPS-5.

Copyright by Kasetsart University All rights reserved

Table 2 Physical properties of porous silica supports and catalysts

Samples	BET surface area (m^2/g)	Pore diameter (nm)	Average pore diameter (nm)	Pore volume (cm^3/g)		NiO crystallite diameter [a] (nm)
				smaller pore	larger pore	
Unloaded porous silica supports						
SBA-15	778	6.5	6.5	0.87		-
Xerogel-5	522	6.5	6.5	0.86		-
MCM-41	996	2.7, 24	17.7	0.76	1.83	-
BPS-5	497	<195, 195	61.2	1.27	0.52	-
Loaded porous silica supports						
Ni/SBA-15	552	6.5	6.5	0.64		18.3
Ni/Xerogel-5	481	6.5	6.5	0.79		11.4
Ni/MCM-41	947	2.7, 21	15.5	0.71	1.64	19.2
Ni/BPS-5	436	<174, 174	42.1	1.11	0.30	16.4

[a] Mean diameter of NiO crystallite determined by XRD using Scherrer equation

Copyright by Kasetsart University All rights reserved

Small angle X-ray scattering analysis was performed to investigate crystalline structure such as shape and size of particle, characteristic distances of partially ordered materials and pore sizes. In the case of SBA-15, it was shown three diffraction peaks at 2θ of 0.9, 1.55 and 1.79 (Figure 28(a)), corresponding to (100), (110), and (200) reflection planes respectively, indicated the existence of well-order 2D hexagonal mesoporous structure (Bérubé and Kaliaguine, 2008; Qu *et al.,* 2010; Jullaphan *et al.,* 2009). For MCM-41, the diffraction peaks at 2θ of 2.71, 4.71 and 5.41 which corresponded (100), (110), and (200) reflection planes respectively were appeared (Figure 28(c)). This indicated the long-range, ordered hexagonal structure of mesoporous MCM-41 (Jomekian *et al.* 2011; Teabpinyok *et al.,* 2012; Chen and Wang, 2002). It should be noted that MCM-41 synthesized using our technique has different structure since the short-range hexagonal structure was obtained. It was observed that, a major peak was shifted to the 2θ of lower than the conventional MCM-41 silicas, indicating the existence of larger pore size of MCM-41. This was corresponding to the result of N_2-sorption analysis as shown in Table 2 and in good agreement with those reported by Kiatphuengporn *et al.* (2014). Moreover, 2 diffraction peaks at higher angles were disappeared, this indicated that the long-range, ordered hexagonal pore structure was reduced (Duarte *et al.,* 2012). In the case of Xerogel-5 and BPS-5, the smaller peaks were disappeared (Figure 28(b) and (d)), while the major peak was shifted to the lower 2θ and peak intensity was significantly decreased, corresponding to the formation of disordered hexagonal structure with larger pore size of these supports.

X-ray diffraction analysis was performed to investigate types of nickel species and average nickel oxide crystallite size. As shown in Figure 29, all catalysts mainly composed of NiO phase only which diffraction peaks appeared at 2θ of 37.35, 43.35, 63, and 75.5 ^{o} corresponding to (111), (200), (220), and (311) planes of cubic phase NiO (Bej *et al.,* 2013). The crystallite sizes of NiO calculated using Scherrer equation were listed in Table 2. It can be seen that NiO on SBA-15 and Xerogel-5 supports were both larger than the pore diameter of these supports. This result implied that the majority of NiO particles could not penetrate into pores of these supports. However, in the case of MCM-41 and BPS-5, the NiO crystallite sizes were smaller than pore

Copyright by Kasetsart University. All rights reserved

diameters, as a result NiO could be possibly deposited in the pores of these supports. Moreover, NiO crystallite sizes over SBA-15, MCM-41 and BPS-5 supports were quite similar.

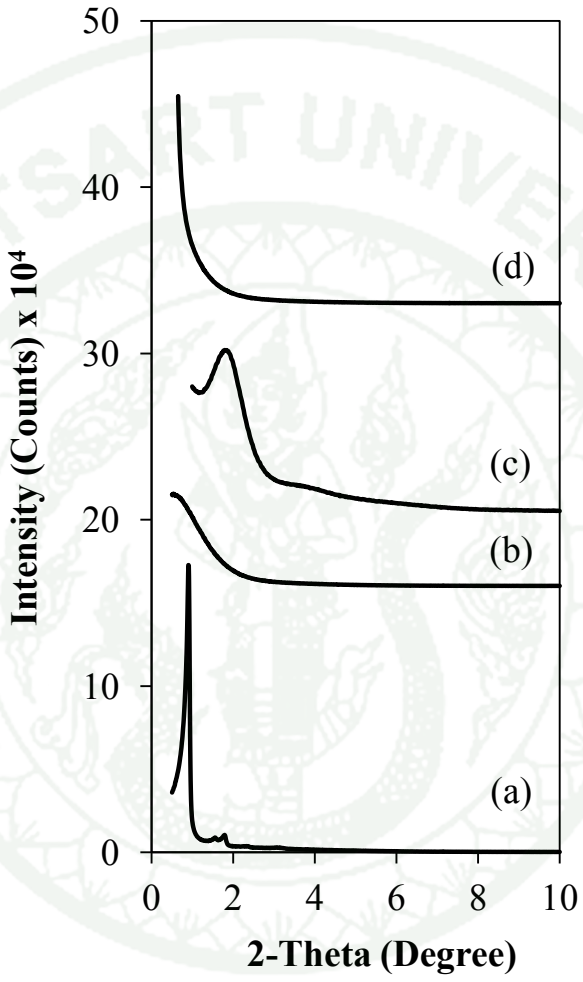

Figure 28 Small angle X-ray scattering (SAXS) patterns of porous silica supports. (a) SBA-15 (b) Xerogel-5 (c) MCM-41 and (d) BPS-5.

Copyright by Kasetsart University All rights reserved

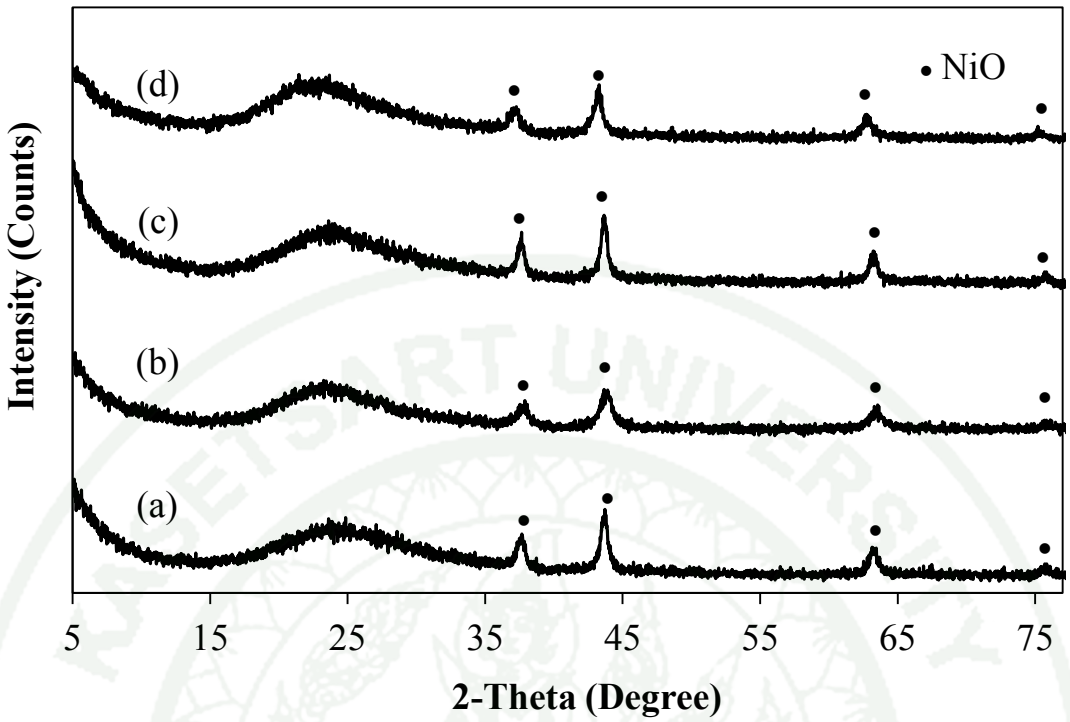

Figure 29 XRD patterns of 5 wt.% Ni on porous silicas supports: (a) Ni/SBA-15 (b) Ni/Xerogel-5 (c) Ni/MCM-41 and (d) Ni/BPS-5.

In order to identify the reduction behavior and metal-support interaction, Temperature programmed reduction (TPR) was applied. Figure 30 shows the result of TPR of 5 wt. % Ni metal loaded on each silica support. Based on the XRD result (Figure 29), it confirmed that the type of nickel metal loaded on silica supports by incipient wetness impregnation was nickel oxide (NiO) only. Bhering *et al.* (2002) reported that NiO could be thoroughly reduced to Ni metal in a single-stage reduction process ($Ni^{2+} \rightarrow Ni^{0}$). In this work, the similar reduction stage of nickel catalyst occurred. However, it was observed that the synthesized catalysts show more than one peaks of reduction temperature due to the different environment of each metal catalyst. The first TPR peak of each catalyst at the lower reduction temperature (372 ^{o}C for Ni/SBA-15, 395 ^{o}C for Ni/BPS-5, 397 ^{o}C for Ni/MCM-41, and 415 ^{o}C for Ni/Xerogel-5) attributed to reduction of bulk NiO with less or no interaction with the supports as confirmed by the reduction temperature of pure nickel oxide (Mile *et al.,*

Copyright by Kasetsart University All rights reserved

1990; Lensveld *et al.,* 2001). This result also implied the existence NiO clusters of the size larger than pore diameters of supports (free NiO clusters).

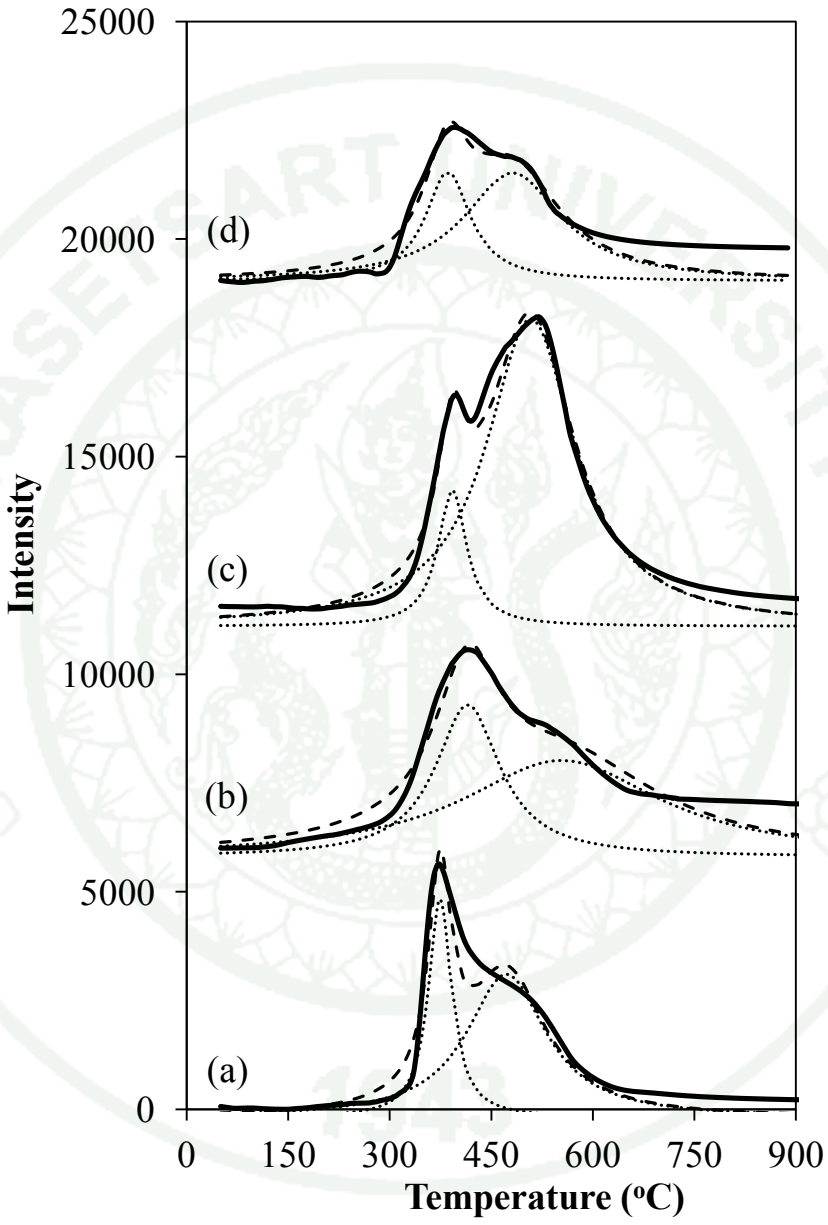

Figure 30 TPR curves of (a) NiO/SBA-15, (b) NiO/Xerogel-5, (c) NiO/MCM-41, and (d) NiO/BPS-5.

TPR profile from experiment — — — TPR profile from program

····· Deconvoluted NiO profile

Copyright by Kasetsart University All rights reserved

The second peak at higher reduction temperature (470 ^{o}C for Ni/SBA-15, 473 ^{o}C for Ni/BPS-5, 520 ^{o}C for Ni/MCM-41, and 535 ^{o}C for Ni/Xerogel-5) could be assigned to reduction of NiO stronger interacted with the support, possibly due to the surface form of nickel on support (Zapata *et al.,* 2010) or the smaller NiO cluster sizes which potentially deposited inside the pores of catalyst support (Mile *et al.,* 1990). It should be note that the smaller NiO crystallite size could lead to the stronger metal-support interaction between NiO and Xerogel-5, resulting in higher reduction temperature than that of SBA-15. Similar trend of result was reported by Goncalves *et al.* (2006). Based on the pore sizes of catalyst supports and NiO crystallite sizes as shown in Table 2, it implied that NiO clusters could possibly deposit on outer surface (could not located into pore) of SBA-15 and Xerogel-5. Comparing between BPS-5 and Xerogel-5 supports, it was found that NiO on BPS-5 required lower reduction temperature owing to its larger sinusoidal pore, leading to larger NiO crystallite size with less metal-support interaction. In the case of MCM-41 and SBA-15 supports, similar mean NiO crystallite sizes were observed. However, for MCM-41, NiO clusters could thoroughly deposit in the pore of MCM-41 support resulting in smaller and segregate NiO clusters with stronger metal-support interaction, while NiO clusters stayed outside the pores of SBA-15 support. As a result, the weaker metal-support interaction was obtained.

The hydrogen uptake used for catalyst reduction could be calculated from TPR peak area as the result shown in Table 3. Hydrogen consumption generally depends on amounts of metal loading, and therefore hydrogen consumption is increased when the loading amount of metal is increased (Kiatphuengporn *et al.,* 2014; Hoang *et al.,* 2011). In this work, different values of hydrogen uptake were observed although each silica support was loaded with the same amount of nickel metal. This result confirmed that the hydrogen uptake not only depends on metal content in the catalyst but also active surface of catalyst; in this case the smaller size the higher hydrogen uptake is observed. In this case of nickel loaded on MCM-41 support, the highest amounts of hydrogen uptake among other supports (5.25 mmol g cat^{-1}) was observed, indicating the highest active surface of nickel over MCM-41 support.

Copyright by Kasetsart University All rights reserved

Table 3 H_2 uptake of Ni catalysts supported on different supports

Catalysts	H_2 uptake	
	mol H_2	mmol g-cat^{-1}
Ni/SBA-15	0.00031	3.08
Ni/Xerogel-5	0.00039	3.92
Ni/MCM-41	0.00052	5.25
Ni/BPS-5	0.00027	2.75

In order to identify the reduction degree of Ni catalyst after reduction K-edge XANES technique was applied. Figure 31(A) and (B) shows Ni K-edge XANES of the Ni catalysts before (fresh catalyst) and after reduction with hydrogen gas (active catalyst), respectively. The XANES spectrums of Ni catalyst were compared to Ni foil and NiO reference, it's shown in Figure 31(A). The spectra of fresh catalyst were similar to that of NiO reference. A small pre-edge signal was observed at 8335 eV, while the two-stage edge was observed at 8341 and 8345 eV (Baudouin *et al.,* 2013). In the case of reduced catalysts at temperature of 600 ^oC as shown in Figure 31(B), similar result to that of Ni foil spectra was observed (the X-ray adsorption edge of a Ni^0 reference occurred in two stages at 8333 and 8345 eV), indicating that the reduced nickel in these catalysts were Ni metal was active for methane cracking reaction (Takenaka *et al.,* 2001). In addition, it was found that the reduction degree of Ni metal on silica supports was possibly greater than 90% at reduction temperature of 600 ^oC for the period of 3 h.

Copyright by Kasetsart University All rights reserved

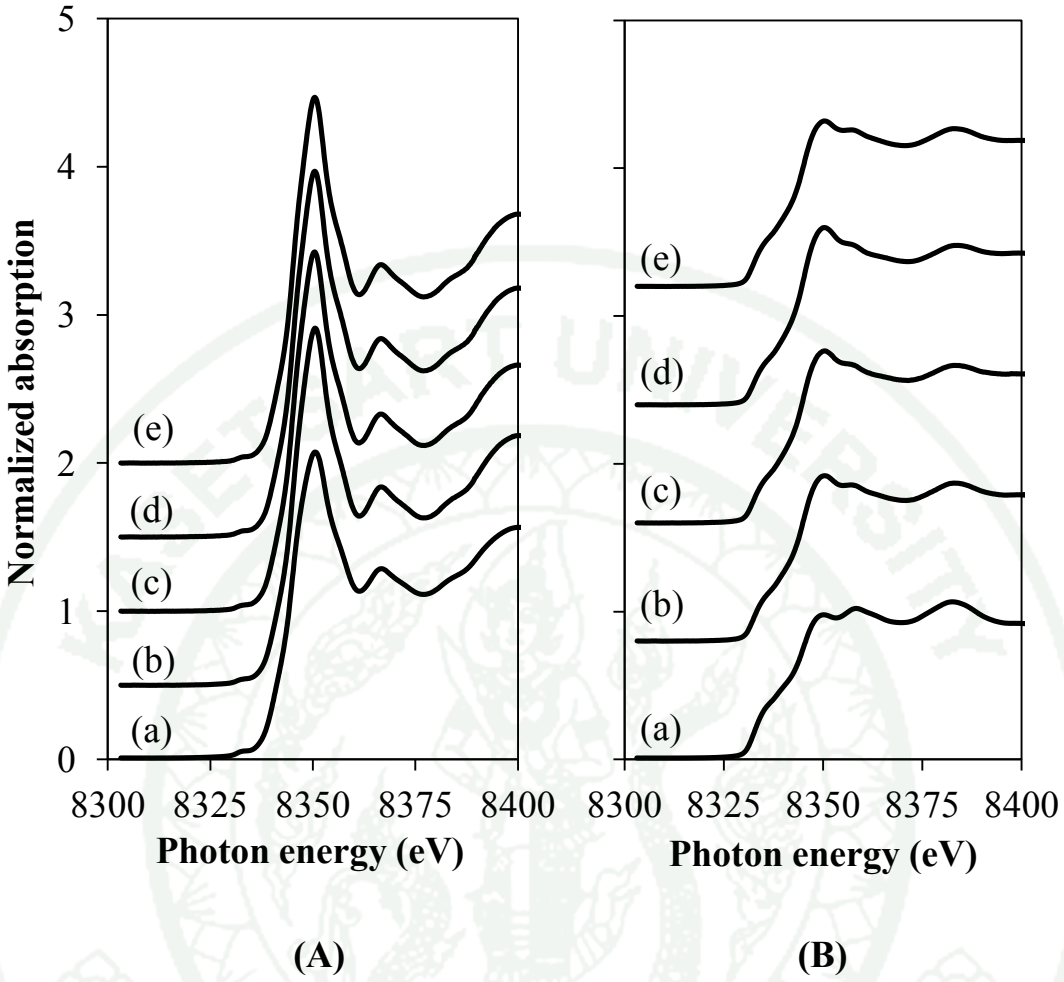

Figure 31 Ni K-edge XANES spectra of nickel on silica supports, NiO and Ni foil (A) fresh nickel catalysts (a) standard NiO (b) Ni/SBA-15 (c) Ni/Xerogel-5 (d) Ni/MCM-41 and (e) Ni/BPS-5 and (B) nickel catalyst reduced at 600 ^{o}C (a) Ni foil (b) Ni/SBA-15 (c) Ni/Xerogel-5 (d) Ni/MCM-41 and (e) Ni/BPS-5.

2. Methane Cracking Reaction

The catalytic performance of nickel catalyst over each silica support in methane cracking reaction was carried out in the catalytic fixed-bed reactor under atmospheric pressure. Figures 32 and 33 showed methane conversion and hydrogen concentration of Ni catalyst over various silica supports at reaction temperatures of 500, 550, 600 and 650 ^{o}C, respectively. Methane conversions were continuously

Copyright by Kasetsart University All rights reserved

decreased with reaction time until the catalysts were completely deactivated. In the temperature range of 500-600 ^{o}C, the order of activity based on the initial methane conversion was Ni/BPS-5 ≈ Ni/MCM-41 > Ni/SBA-15 > Ni/Xerogel-5. After 15 minute time on stream, the conversions were rapidly decreased. The order of activity was Ni/BPS-5 > Ni/MCM-41 > Ni/SBA-15 > Ni/Xerogel-5. However, at higher reaction temperature (650 ^{o}C), no significant differences in the methane conversion among each catalyst were observed.

Furthermore, the time period for complete deactivation (longest life time) of each catalyst was obviously different at relatively lower reaction temperature (500-600 ^{o}C). Ni/BPS-5 catalyst exhibited the longest time period, followed by Ni/MCM-41, Ni/SBA-15, and Ni/Xerogel-5 catalysts. This could be attributed to the relatively larger pore size and pore volume of Ni/BPS-5 and Ni/MCM-41 catalysts compared to those of Ni/SBA-15 and Ni/Xerogel-5 catalysts. In addition, it was found that the pore characteristic had an effect on prolonging the life time of catalysts as the straight pore was more preferable than the sinusoidal pore.

A similar trend of results was observed on H_2 yield (Figure 6). The highest yield of H_2 was obtained from Ni/BPS-5 and followed by Ni/MCM-41, Ni/SBA-15, and Ni/Xerogel-5 catalysts, consecutively. At the temperature of 600-650 ^{o}C, all catalysts were rapidly deactivated and H_2 yields were abruptly decreased to lower than 1 % within 50 min time on stream. It could be explained that at higher reaction temperature, the atomic carbon could potentially accumulate on the surface of active metallic nickel since at the moment the nucleation rate was faster than the carbon diffusion rate through nickel cluster. However, at lower reaction temperature (500-550 ^{o}C), the nucleation rate was slower than the carbon diffusion rate through nickel cluster (Zhang and Amiridis, 1998; Suelves *et al.,* 2005). Moreover, it was found that at this reaction temperature range (500-650 ^{o}C), this methane cracking reaction led to the formation of carbon filaments (Borghei *et al.,* 2010).

Copyright by Kasetsart University All rights reserved

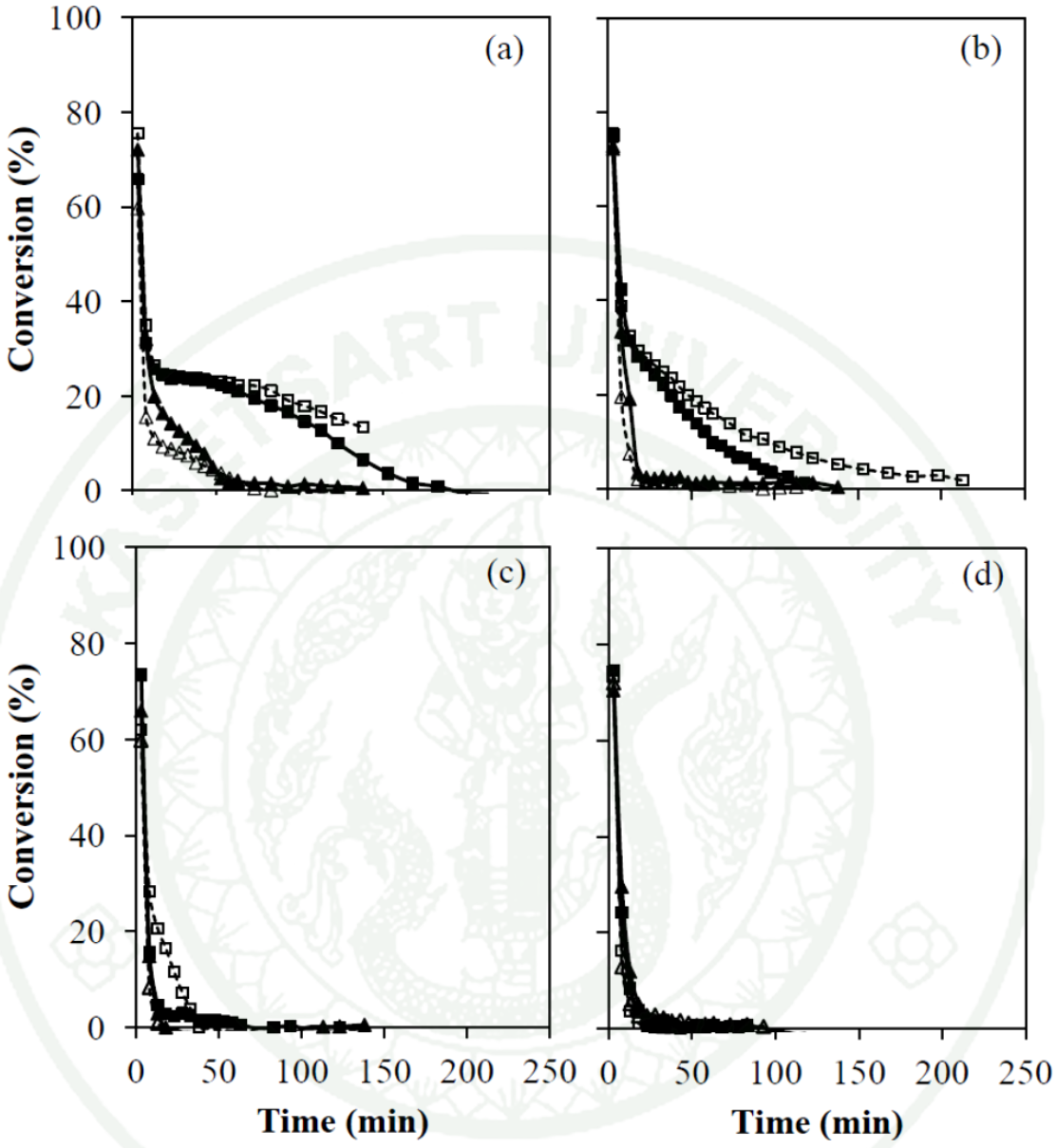

Figure 32 CH_4 conversion in the CH_4 cracking over Ni catalysts supported on different supports at (a) 500 °C (b) 550 °C (c) 600 °C and (d) 650 °C.

Ni/SBA-15 Ni/Xerogel-5

Ni/MCM-41 Ni/BPS-5

Copyright by Kasetsart University All rights reserved

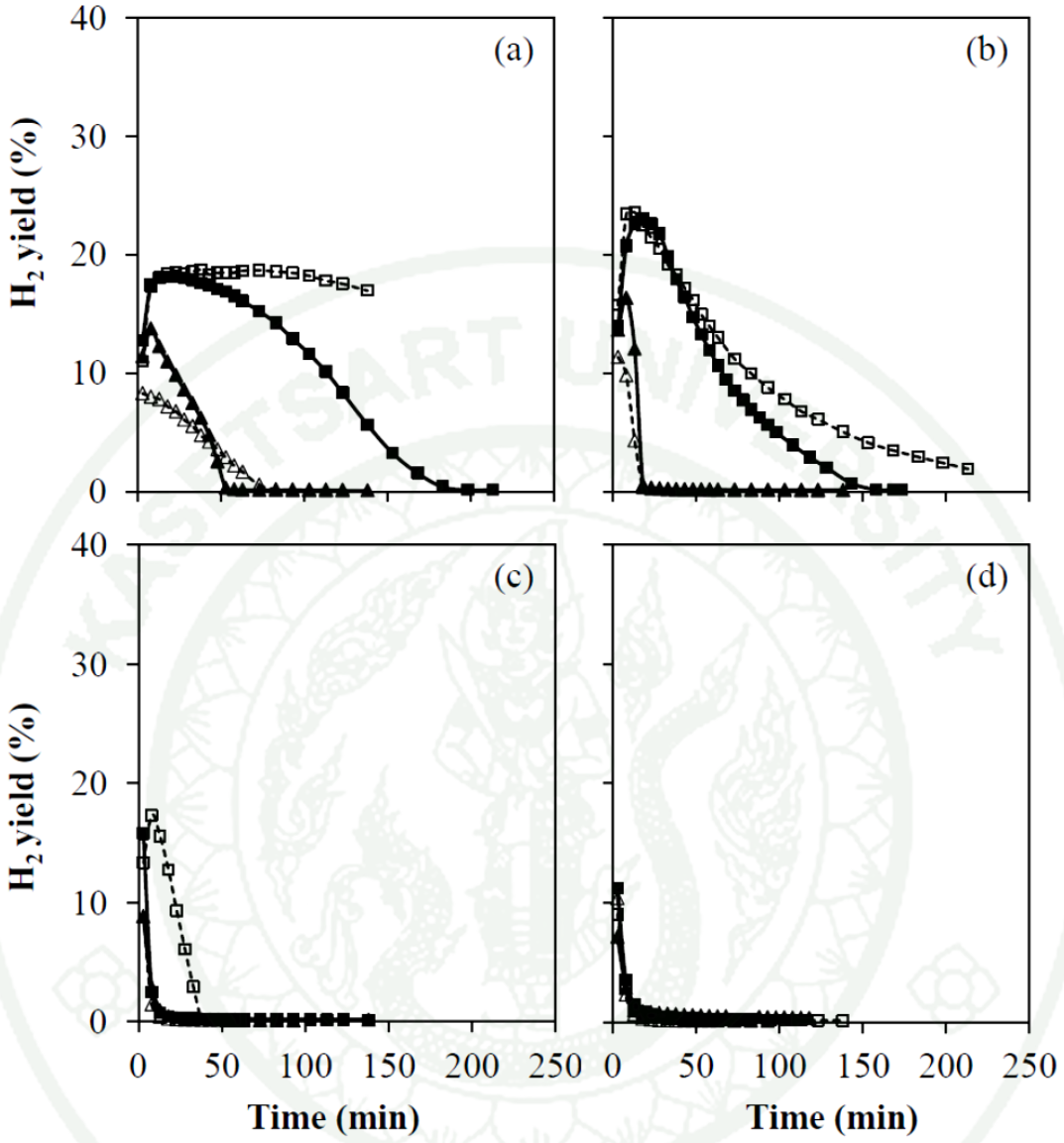

Figure 33 H_2 yield in the CH_4 cracking over Ni catalysts supported on different supports at (a) 500 °C (b) 550 °C (c) 600 °C and (d) 650 °C.

Ni/SBA-15 Ni/Xerogel-5

Ni/MCM-41 Ni/BPS-5

In order to investigate the morphology of catalyst surface after reaction (used catalyst), SEM technique was applied. The catalyst was deactivated at all reaction temperatures by carbon formed would partially cover the active nickel clusters and pore of catalyst, as a result, the reactant gas (CH_4) could hardly be cracked to form hydrogen and carbon products on active nickel surface. SEM images of the used

Copyright by Kasetsart University All rights reserved

catalysts in methane cracking reaction at temperature of 500 ^{o}C were shown in Figure 34. It was found that the allotrope of carbon that covered the catalyst surface was carbon filaments. The mechanism of carbon filaments formation was explained as follows: After methane was adsorbed on the active site and cracked to hydrogen and carbon, carbon deposited on nickel surface then dissolved into nickel formed a layer of uniform concentration solution of carbon and consecutively diffused through the nickel particle to nickel-support interface until the carbon solution of nickel was super-saturated. At the moment, nucleation of carbon filament was begun (Yang and Chen, 1989; Snoeck *et al.,* 1997). In addition, at the tips of carbon filaments appeared Ni metal clusters and the diameter of carbon filaments was controlled by the size of Ni metal clusters.

TGA technique was used to investigate the amounts and types of the product carbon species. It should be noted that in this work the catalysts were mixed with inert sand and packed in the inconel tube reactor, therefore a separation of used catalyst from sand was not possible, thus only qualitative data regarding the types of carbon was reported. TGA and differential thermal analysis (DTA) result of all used catalysts after methane cracking reaction at temperature of 500, 550, 600 and 650 °C are shown in Figures 35 and 36, respectively. As shown in Figures 35 and 36, the TGA and DTA curves exhibited a two-step weight loss. The first step at temperature below 100 °C represented the residual moisture in the used catalyst. The second step at the temperature range of 500-630 ^{o}C was the decomposition of carbon nanofibers (CNFs) which in good agreement with those reported by Ghosh *et al.* (2008) and Kumar *et al.* (2007). However, it was observed that the second step of some used catalysts exhibited two peaks of derivative weight loss. These two peaks implied the decomposition of CNFs with different diameters. The large size CNFs were decomposed at lower temperature than small size (Scheibe *et al.,* 2010; Mathur *et al.,* 2008).

Moreover, it was found that percentage of weight loss of the used catalysts at higher reaction temperature (600-650 ^{o}C) was lower than those of at lower reaction

Copyright by Kasetsart University. All rights reserved

temperature (500-550 ^{o}C). It could be attributed to the fact that, the amount of CNFs synthesized at higher temperature was less than those synthesized at lower temperature. At high reaction temperature, the catalyst was rapidly deactivated resulting in the carbon filaments formed on catalyst had a little and short length (Rahman *et al.,* 2006). In addition, the large pore size and pore volume of catalysts (Ni/MCM-41 and Ni/BPS-5) gave amount of CNFs more than the catalyst has small pore size and pore volume (Ni/Xerogel-5 and Ni/SBA-15).

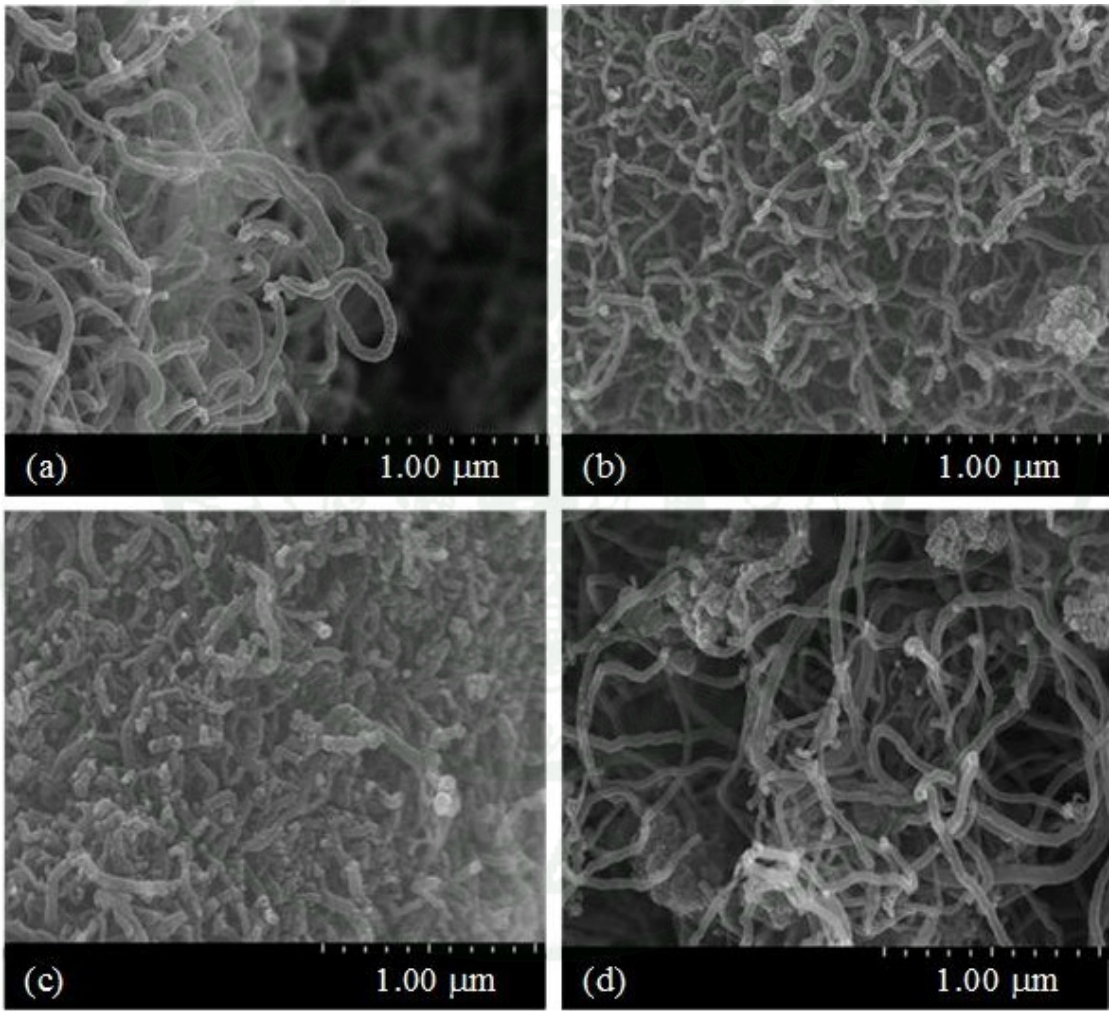

Figure 34 SEM images of catalysts after the complete deactivation at 500 ^{o}C: (a) Ni/SBA-15, (b) Ni/xerogel-5, (c) Ni/MCM-41, and (d) Ni/BPS-5.

Copyright by Kasetsart University All rights reserved

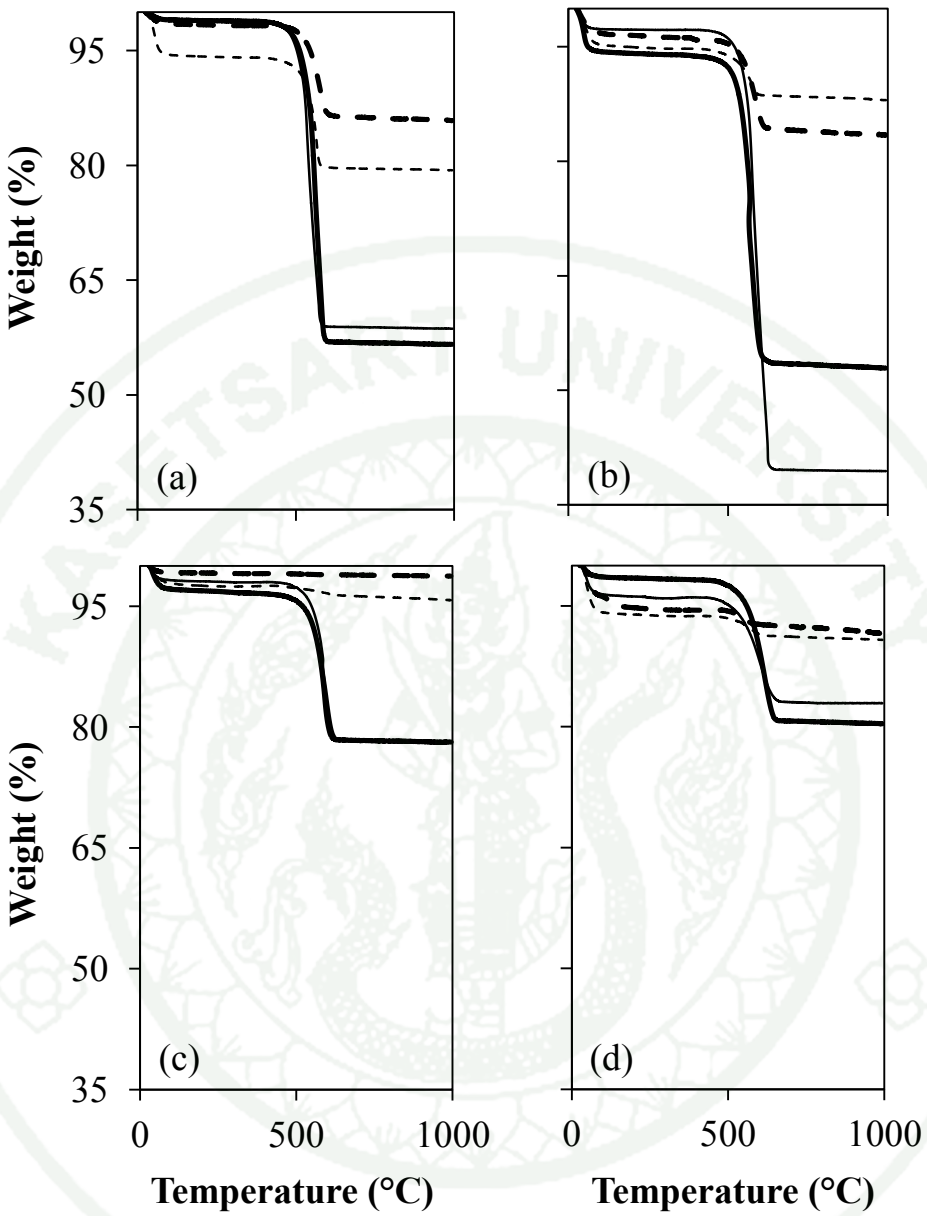

Figure 35 TGA curves of catalysts after CH_4 cracking reaction at (a) 500 ^oC (b) 550 ^oC (c) 600 ^oC and (d) 650 ^oC.

- Ni/SBA-15
- Ni/Xerogel-5
- Ni/MCM-41
- Ni/BPS-5

Copyright by Kasetsart University All rights reserved

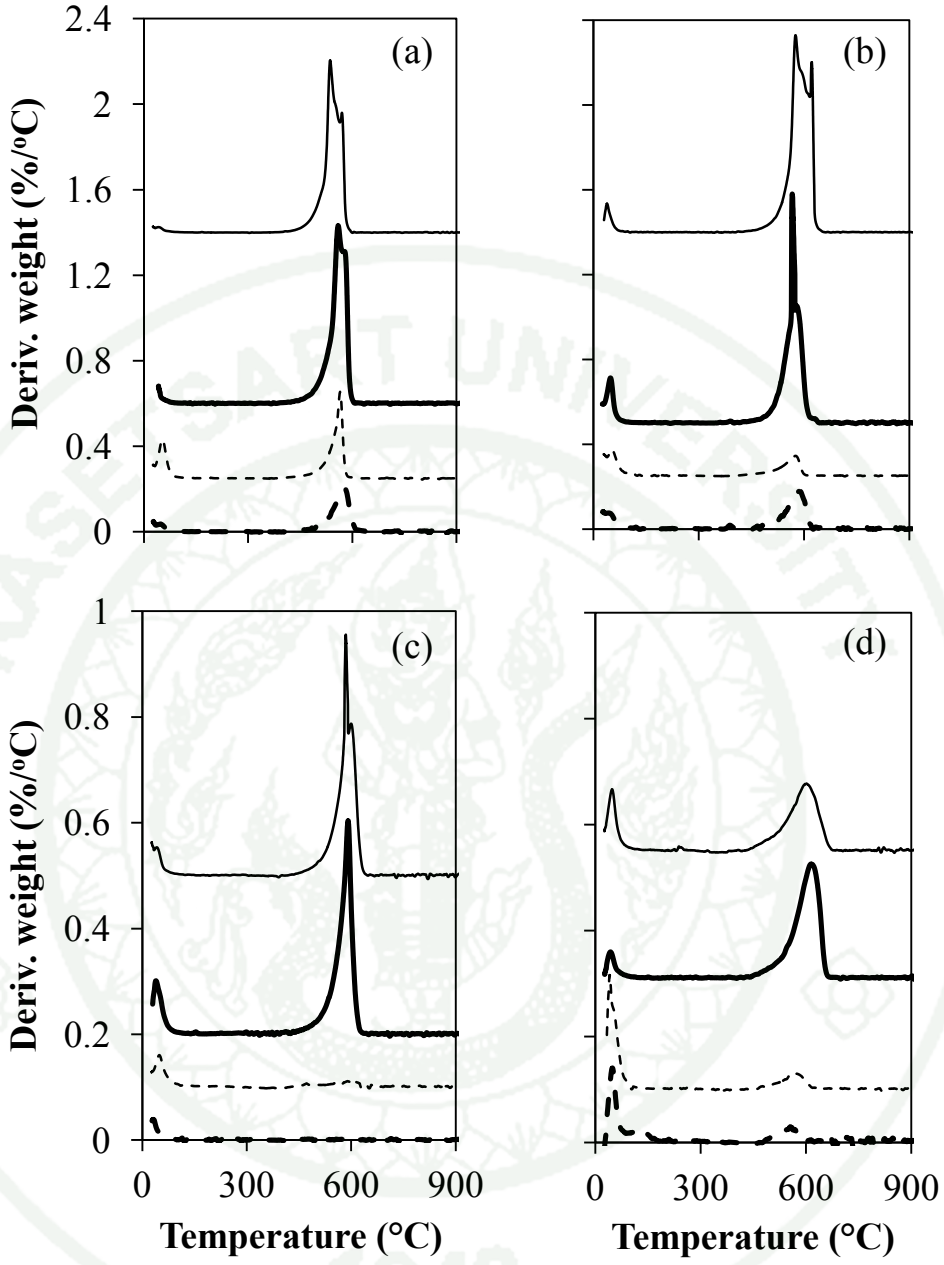

Figure 36 DTA curves of catalysts after CH_4 cracking reaction at (a) 500 °C (b) 550 °C (c) 600 °C and (d) 650 °C.

Copyright by Kasetsart University All rights reserved

In order to obtain more information on carbon filaments formed on the catalyst surface, Raman spectroscopy was applied to investigate the used catalysts. Figure 37(A) and (B) shows Raman spectra of carbon formed on the catalysts by methane cracking reaction at temperatures of 500 and 650 ^{o}C, respectively. The characteristic peak of D band (~1329 cm^{-1}) and G (~1582 cm^{-1}) band were observed for all used catalysts. The D band indicated the structural imperfection of graphite, whereas the G band was attributed to the in-plane carbon-carbon stretching vibrations of graphite layers with uniform graphite structure, respectively (Takenaka *et al.,* 2003). It was observed that the G band of used Ni/MCM-41 at reaction temperature of 500^{o}C was shifted to left (1575 cm^{-1}) due to the formation of large-size CNFs while that of used Ni/BPS-5 was shifted to right (1588 cm^{-1}) due to the formation of small-size CNFs (Wang *et al.,* 2002).

In addition, the intensity ratio between D and G bands (I_D/I_G) was enhanced when the reaction temperature was decreased. At high reaction temperature, I_D/I_G range of 0.78–1.11, the graphitic order of CNFs was greater than CNFs synthesized at low reaction temperature (I_D/I_G range of 1.38–1.57) (Jawhari *et al.* 1995). Moreover, the graphitic order of CNFs on each catalyst was different. At 500 ^{o}C, the order of CNFs was Ni/MCM-41 (I_D/I_G = 1.38) > Ni/BPS-5 (I_D/I_G = 1.45) > Ni/SBA-15 (I_D/I_G = 1.50) > Ni/Xerogel-5 (I_D/I_G = 1.57). However, at high temperature (650 ^{o}C), the order of CNFs over Ni/Xerogel-5 (I_D/I_G = 0.78) > Ni/BPS-5 (I_D/I_G = 0.87) > Ni/MCM-41 (I_D/I_G = 0.93) > Ni/SBA-15 (I_D/I_G = 1.11) catalysts was observed.

Copyright by Kasetsart University All rights reserved

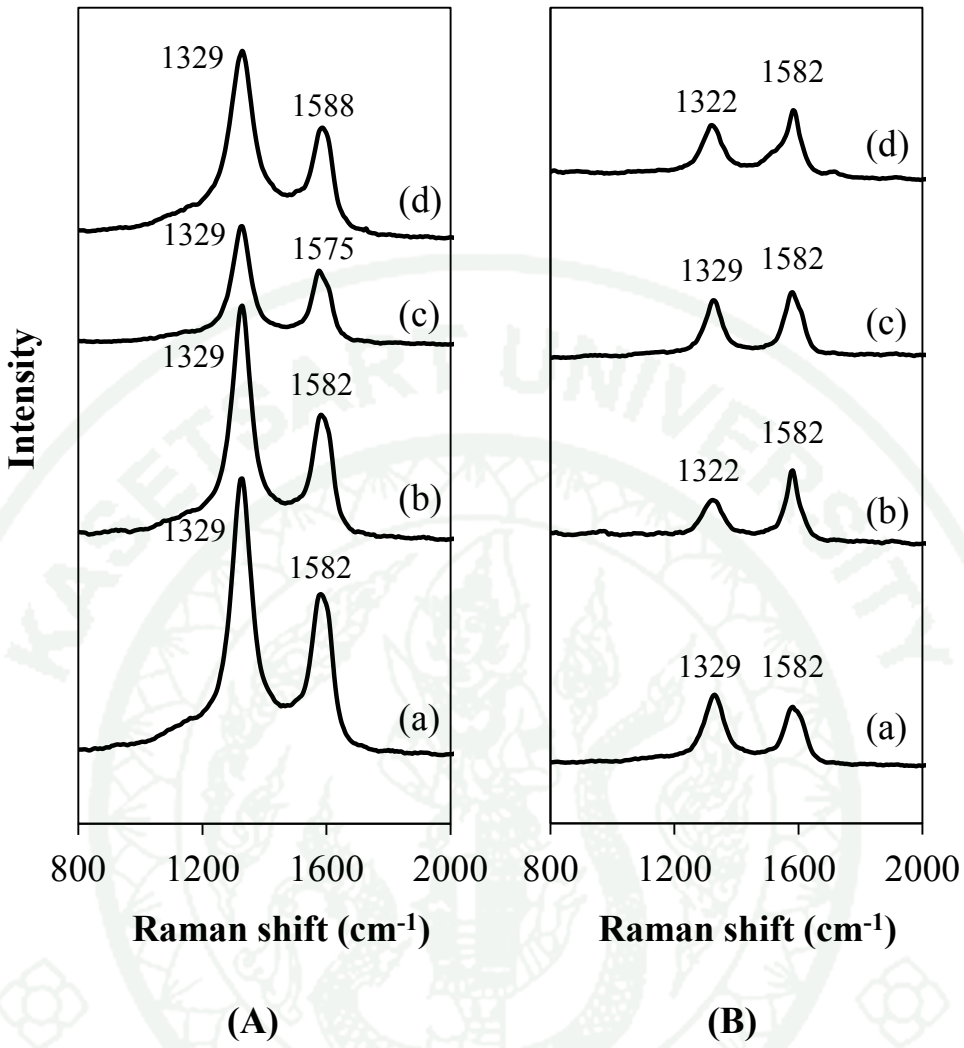

Figure 37 Raman spectra of catalysts after CH_4 cracking reaction at (A) 500 ^oC and (B) 650 ^oC (a) Ni/SBA-15 (b) Ni/Xerogel-5 (c) Ni/MCM-41 and (d) Ni/BPS-5.

From the result of performance of catalyst in methane cracking reaction (Figure 32), it can be seen that reaction performance relies on rate of diffusion of reactant into pores of catalyst and product gases released from pores of catalyst. The significant parameter affecting the rate of diffusion is gas diffusivity. In the case of porous pellet catalyst, the diffusion of gas in pore is taken place because of concentration gradients by the reaction (reactant gas is converted to product at active site). Thus, the model for used prediction the rate of gas diffusion could involve pore structure, led to effective diffusion (Fogler, 2004). The calculated effective diffusion

Copyright by Kasetsart University All rights reserved

coefficients are shown in Table 4. From Figure 32 and Table 4, it was observed that efficiency of catalysts in methane cracking reaction was increased with increasing effective diffusion coefficient value. For calculated effective diffusion coefficients were obtained from Equation (6), (7), (8) and (9) as shown below (McCabe *et al.,* 2005).

$$D_e = D_{pore}\varepsilon/\tau \quad (6)$$

where, ε and τ are porosity and tortuosity of catalyst, respectively and D_{pore} represents diffusivity of methane in pore which obtains from:

$$1/D_{pore} = 1/D_{AB} + 1/D_K \quad (7)$$

where, D_{AB} and D_K are bulk diffusivity (cm^2/s) and Knudsen diffusivity (cm^2/s), respectively. These could be calculated from:

$$D_{AB} = 0.001858T^{3/2}[(M_{CH_4}+ M_{N_2})/(M_{CH_4}M_{N_2})]^{1/2}/[P(\sigma_{CH_4N_2})^2\Omega_D] \quad (8)$$

$$D_K = 9700\ r\ (T/M)^{1/2} \quad (9)$$

where, T = temperature (K)

M_{CH_4} = molecular weight of CH_4

M_{N_2} = the molecular weight of N_2

P = the total pressure (atm)

$\sigma_{CH_4N_2}$ = the effective collision diameter (Å)

Ω_D = the collision integral

r = the pore radius (cm)

For Equation (6), tortuosity value on catalyst could be calculated from Equation (10), given by Beekman (1990) for heterogeneous catalyst as follows (Table 4)

Copyright by Kasetsart University All rights reserved

$$\tau = \varepsilon/[1 - (1 - \varepsilon)^{1/3})] \quad (10)$$

Comparing between Ni/BPS-5 and Ni/Xerogel-5, the pore structure of both catalysts was sinusoidal pore. It was observed that the effective diffusion coefficient of Ni/BPS-5 was higher than Ni/Xerogel-5 because Ni/BPS-5 has larger pore size, leading to higher diffusion rate of reactant and product gases. As a result, the higher catalytic performance in methane cracking reaction was obtained with Ni/BPS-5 catalyst. In the case of Ni/SBA-15 and Ni/Xerogel-5, the both catalysts had the same pore size but different pore structure Accordingly, Ni/SBA-15 catalyst with straight pore exhibited slightly higher effective diffusion coefficient than that of Ni/Xerogel-5 catalyst with sinusoidal pore. From this data, it confirmed that the larger pore size and straight pore structure of catalyst led to the higher methane conversion. In addition, we expected that Ni/BPS-5 consisted of macro porous resulting in pore blockage of carbon filaments is slower than small pore because large pore volume could support a lot of carbon therefore; require a long time to block the pores of the catalyst completely.

Table 4 Methane diffusivity in pore of Ni catalysts supported on different supports

Catalysts	Porosity	Tortuosity	Effective diffusion coefficient [a] (cm^2/s)
Ni/SBA-15	0.60	2.28	0.006
Ni/Xerogel-5	0.59	2.30	0.005
Ni/MCM-41	0.85	1.80	0.024
Ni/BPS-5	0.75	2.02	0.047

[a] Diffusivity reaction temperature corresponding to maximum methane conversion (500 ^{o}C)

Copyright by Kasetsart University All rights reserved

CONSLUSIONS

In this research, 5 wt.% nickel was loaded on BPS-5, MCM-41, Xerogel-5, and SBA-15 by incipient wetness impregnation technique. The physicochemical properties of the catalysts were investigated in order to identify appropriate pore characteristic and operating temperature for CH_4 cracking reaction. The results of the experiment can be summarized as follows:

1. The life time of the catalyst depended on the pore characteristic of each support. The larger pore size of the catalyst the longer life time was obtained. Ni/BPS-5 with the largest macropore size of 174 nm exhibited the longest life time for 250 minute. Moreover, on the basis of same pore size, the straight pore structure gave the higher CH_4 conversion compared to the sinusoidal pore structure.

2. After 15 minute time on stream, CH_4 conversion of Ni loaded on bimodal porous silica supports (Ni/BPS-5 and Ni/MCM-41) was gradually decreased in the operating temperature ranges of 500-550 ^oC while such CH_4 conversion was rapidly decreased at higher temperature (600-650 ^oC). However, for Ni loaded on monomodal porous silica supports (Ni/SBA-15 and Ni/Xerogel-5), CH_4 conversion was rapidly decreased for all temperature periods.

3. The CNFs were formed on the catalyst surface in all ranges of the operating temperature. The higher amount of CNFs was obtained when CH_4 cracking reaction was operated at lower temperature (500-550 ^oC) compared to higher temperature (600-650 ^oC) for all catalysts. In Addition, an increasing in the operating temperature enhanced the graphitic order of CNFs.

Copyright by Kasetsart University All rights reserved

LITERATURE CITED

Abbas, H.F. and W.M.A.W. Daud. 2010. Hydrogen production by thermocatalytic decomposition of methane using a fixed bed activated carbon in a pilot scale unit: Apparent kinetic, deactivation and diffusional limitation studies. **International Journal of Hydrogen Energy** 35: 12268-12276.

Aiello, R., J.E. Fiscus, H.C. Loye and M.D. Amiridis. 2000. Hydrogen production via the direct cracking of methane over Ni/SiO_2: catalyst deactivation and regeneration 192: 227 - 234. **Applied Catalysis A: General** 192: 227-234.

Alstrup, I. 1988. A new model explaining carbon filament growth on nickel, iron, and Ni-Cu alloy catalysts. **Journal of Catalysis** 109: 241-251.

Amin, A.M., E. Croiset, C. Constantinou and W. Epling. 2012. Methane cracking using Ni supported on porous and non-porous alumina catalysts. **International Journal of Hydrogen Energy** 37: 9038-9048.

Ashok, J., S.N. Kumar, A. Venugopal, V.D. Kumari and M. Subrahmanyam. 2007. CO_x-free H2 production via catalytic decomposition of CH_4 over Ni supported on zeolite catalysts. **Journal of Power Sources** 164: 809-814.

Avdeeva, L.B., D.I. Kochubey and Sh.K. Shaikhutdinov. 1999. Cobalt catalysts of methane decomposition: accumulation of the filamentous carbon. **Applied Catalysis A: General** 177: 43-51

Awadallah, A.E., A.A. Aboul-Enein and A.K. Aboul-Gheit. 2014. Effect of progressive Co loading on commercial Co–Mo/Al_2O_3 catalyst for natural gas decomposition to CO_x-free hydrogen production and carbon nanotubes. **Energy Conversion and Management** 77: 143-151.

Copyright by Kasetsart University All rights reserved

Baudouin, D., U. Rodemerck, F. Krumeich, A. de Mallmann, K.C. Szeto, H. Ménard, L. Veyre, J.P. Candy, P.B. Webb, C. Thieuleux and C. Copéret. 2013. Particle size effect in the low temperature reforming of methane by carbon dioxide on silica-supported Ni nanoparticles. **Journal of Catalysis** 297: 27-34.

Beeckman, J.W. 1990. Mathematical description of heterogeneous materials. Chemical Engineering Science 45: 2603-2610.

Bej, B., N.C. Pradhan and S. Neogi. 2013. Production of hydrogen by steam reforming of methane over alumina supported nano-NiO/SiO_2 catalyst. **Catalysis Today** 207: 28-35.

Bérubé, F. and S. Kaliaguine. 2008. Calcination and thermal degradation mechanisms of triblock copolymer template in SBA-15 materials. **Microporous and Mesoporous** Materials 115: 469-479.

Bhering, D.L., M. Nele, J.C. Pinto and V.M.M. Salim. 2002. Preparation of high loading silica-supported nickel catalyst: analysis of the reduction step. **Applied Catalysis A: General** 234: 55-64.

Bokx, P.K., A.J.H.M. Kock, E. Boellaard, W. Klop and J.W. Geus. 1985. The Formation of Filamentous Carbon on iron and Nickel Catalysts I. Thermodynamics. **Journal of Catalysis** 96: 454-467.

Bonura, G., O.D. Blasi, L. Spadaro, F. Arena and F. Frusteri. 2006. A basic assessment of the reactivity of Ni catalysts in the decomposition of methane for the production of "COx-free" hydrogen for fuel cells application. **Catalysis Today** 116: 298-303.

Borghei, M., R. Karimzadeh, A. Rashidi and N. Izadi. 2010. Kinetics of methane decomposition to CO_x-free hydrogen and carbon nanofiber over Ni-Cu/MgO catalyst. **International Journal of Hydrogen Energy** 35: 9479-9488.

Copyright by Kasetsart University All rights reserved

Chen, H. and Y. Wang. 2002. Preparation of MCM-41 with high thermal stability and complementary textural porosity. **Ceramics International** 28: 541-547.

_____, J., M. He, G. Wang, Y. Li and Z.J. Zhu. 2009. Production of hydrogen from methane decomposition using nanosized carbon black as catalyst in a fluidized-bed reactor. **International Journal of Hydrogen Energy** 34: 9730-9736.

Choudhary, T.V., C. Sivadinarayana, C.C. Chusuei, A. Klinghoffer and D.W. Goodman. 2001. Hydrogen Production via Catalytic Decomposition of Methane. **Journal of Catalysis** 199: 9-18.

Duarte, P., D.P. Ferreira, T.F. Lopes, J.V. Pinto, I.M. Fonseca, I.F. Machado and L.F.V. Ferreira. 2012. DSM as a probe for the characterization of modified mesoporous silicas. **Microporous Mesoporous Matererials** 161: 139-147.

Echegoyen, Y., I. Suelves, M.J. Lázaro, R. Moliner and J.M. Palacios. 2007. Hydrogen production by thermo-catalytic decomposition of methane over Ni-Al and Ni-Cu-Al catalysts: effect of calcination temperature. **Journal of Power Sources** 169: 150 - 157.

Ermakova, M.A., D.Y. Ermakov, G.G. Kuvshinov and L.M. Plyasova. 1999. New Nickel Catalysts for the Formation of Filamentous Carbon in the Reaction of Methane Decomposition. **Journal of Catalysis** 187: 77-84.

_____, _____ and _____. 2000. Effective catalysts for direct cracking of methane to produce hydrogen and filamentous carbon: Part I. Nickel catalysts. **Applied Catalysis A: General** 201: 61-70.

Fogler, H.S. 2004. Elements of Chemical Reaction Engineering. 3th ed. **Prentice-Hall International, Inc**. United States.

Copyright by Kasetsart University All rights reserved

Ghosh, P., T. Soga, K. Ghosh, T. Jimbo, R. Katoh, K. Sumiyama and Y. Ando. 2008. Effect of sulfur concentration on the morphology of carbon nanofibers produced from a botanical hydrocarbon. **Nanoscale Research Letters** 3: 242-248.

Goncalves, G., M.K. Lenzi, O.A.A. Santos and L.M.M. Jorge. 2006. Preparation and characterization of nickel based catalysts on silica, alumina and titania obtained by sol-gel method. **Journal of Non-Crystalline Solids** 352: 3697-3704.

Guevara, J.C., J.A. Wang, L.F. Chen, M.A. Valenzuela, P. Salas, A.G. Ruiz, J.A. Toledo, M.A.C. Jácome, C.A. Chavez and O. Novaro. 2010. Ni/Ce-MCM-41 mesostructured catalysts for simultaneous production of hydrogen and nanocarbon via methane decomposition. **International Journal of Hydrogen Energy** 35: 3509-3521.

Hoang, D.L., T.T.H. Dang, J. Engeldinger, M. Schneider, J. Radnik, M. Richter and A. Martin. 2011. TPR investigations on the reducibility of Cu supported on Al_2O_3, zeolite Yand SAPO-5. **Journal of Solid State Chemistry** 184: 1915-1923.

Ichioka, H., N. Higashi, Y. Yamada, T. Miyake and T. Suzuk. 2007. Carbon nanotube and nanofiber syntheses by the decomposition of methane on group 8-10 metal loaded MgO catalyst. **Diamond and Related Materials** 16: 1121 - 1125.

Iler, R.K. 1979. The chemistry of silica: Solubility, polymerization, colloid and surface properties, and biochemistry. **John Wiley Sons Inc**. United States.

Jawhari, T., A. Roid and J. Casado. 1995. Raman Spectroscopic characterization of some commercially available carbon black materials. **Carbon** 33: 1561-1565.

Copyright by Kasetsart University All rights reserved

Jomekian, A., M. Pakizeh, A.R. Shafiee and S.A.A Mansoori. 2011. Fabrication or preparation and characterization of new modified MCM-41/PSf nanocomposite membrane coated by PDMS. **Separation and Purification Technology** 80: 556-565.

Jullaphan, O., T. Witoon and M. Chareonpanich. 2009. Synthesis of mixed-phase uniformly infiltrated SBA-3-like in SBA-15 bimodal mesoporous silica from rice husk ash. **Materials Letters** 63: 1303–1306.

Kiatphuengporn, S., M. Chareonpanich and J. Limtrakul. 2014. Effect of unimodal and bimodal MCM-41 mesoporous silica supports on activity of Fe–Cu catalysts for CO2 hydrogenation. **Chemical Engineering Journal** 240: 527-533.

Kock, A.J.H.M., P.K. de Bokx, E. Boellaard, W. Klop and J.W. Geus. 1985. The formation of filamentous carbon on iron and nickel catalysts: II. Mechanism. **Journal of Catalysis** 96: 468-480.

Kumar, S., T. Rath, R.N. Mahaling, C.S. Reddy, C.K. Das and K.N. Pandey. 2007. Study on mechanical, morphological and electrical properties of carbon nanofiber/polyetherimide composites. **Materials Science and Engineering B** 141: 61-70.

Lázaro, M.J., Y. Echegoyena, C. Alegrea, I. Suelvesa, R. Molinera and J.M. Palaciosb. 2008. TiO_2 as textural promoter on high loaded Ni catalysts for methane decomposition. **International Journal of Hydrogen Energy** 33: 3320-3329.

Lee, K.K., G.Y. Han, K.J. Yoon and B.K. Lee. 2004. Thermocatalytic hydrogen production from the methane in a fluidized bed with activated carbon catalyst. **Catalysis Today** 93-95: 81-86.

Copyright by Kasetsart University All rights reserved

Lee, E.K., S.Y. Lee, G.Y. Han, B.K. Lee, T.J. Lee, J.H. Jun and K.J. Yoon. 2004. Catalytic decomposition of methane over carbon blacks for CO_2-free hydrogen production. **Carbon** 42: 2641-2648.

Lensveld, D.J., J.G. Mesu, A.J. van Dillen and K.P. de Jong. 2001. Synthesis and characterization of MCM-41 supported nickel oxide catalysts. **Microporous Mesoporous Materials** 44-45: 401-407.

Li, Y., B. Zhang, X. Tang, Y. Xu and W. Shen. 2006. Hydrogen production from methane decomposition over Ni/CeO_2 catalysts. **Catalysis Communications** 7: 380-386.

_____, J. Chen, Y. Qin and L. Chang. 2000. Simultaneous Production of Hydrogen and Nanocarbon from Decomposition of Methane on a Nickel-Based Catalyst. **Energy & Fuels** 14: 1188-1194.

Malaika, A., B. Krzyżyńska and M. Kozłowski. 2010. Catalytic decomposition of methane in the presence of in situ obtained ethylene as a method of hydrogen production. **International Journal of Hydrogen Energy** 35: 7470-7475.

Mathur, R.B., S. Chatterjee and B.P. Singh. 2008. Growth of carbon nanotubes on carbon fibre substrates to produce hybrid/phenolic composites with improved mechanical properties. **Composites Science and Technology** 68: 1608-1615.

McCabe, W.L., J.C. Smith and P. Harriott. 2005. Unit operations of chemical engineering. 7th ed. **McGraw-Hill**. New York.

Mile, B., D. Stirling and M.A. Zammitt. 1990. TPR studies of the effects of preparation conditions on supported nickel catalysts. **Journal of Molecular Catalysis** 62:179-98.

Copyright by Kasetsart University All rights reserved

Morales, J.M, J. Latorre, C. Guillem, A.B. Porter, D.B. Porter and P. Amorós. 2005. Scale-up low-cost synthesis of bimodal mesoporous silicas. **Solid State Sciences** 7: 415-421.

Muradov, N. 2001. Hydrogen via methane decomposition: an application for decarbonization of fossil fuels. **International Journal of Hydrogen Energy** 26: 1165-1175.

_____, F. Smith and A.T. Raissi. 2005. Catalytic activity of carbons for methane decomposition reaction. **Catalysis Today** 102-103: 225-233.

_____, _____, _____ and C. Huang. 2006. Autothermal catalytic pyrolysis of methane as a new route to hydrogen production with reduced CO_2 emissions. **Catalysis Today** 116: 281-288.

Nuernberg, G.B., H.V. Fajardo, D.Z. Mezalira, T.J. Casarin, L.F.D. Probst and N.L.V. Carreño. 2008. Preparation and evaluation of Co/Al_2O_3 catalysts in the production of hydrogen from thermo-catalytic decomposition of methane: Influence of operating conditions on catalyst performance. **Fuel** 87: 1698-1704.

_____, E.L. Foletto, C.E.M. Campos, H.V. Fajardo, N.L.V. Carreñoe and L.F.D. Probst. 2012. Direct decomposition of methane over Ni catalyst supported in magnesium aluminate. **Journal of Power Sources** 208: 409-414.

Niu, Z. and Y. Fang. 2007. Effects of composition of catalysts on the preparation of single-walled carbon nanotubes synthesized over W-Co-MgO catalysts. **Superlattices and Microstructures** 41: 62-70.

Otsuka, K., S. Kobayashi and S. Takenaka. 2000. Decomposition and regeneration of methane in the absence and the presence of a hydrogen-absorbing alloy $CaNi_5$. **Applied Catalysis A: General** 190: 261-268.

Copyright by Kasetsart University All rights reserved

Pinilla, J.L., D. Torres, M.J. Lázaro, I. Suelves, R. Moliner, I. Cañadas, J. Rodríguez, A. Vidal and D. Martínez. 2012. Metallic and carbonaceous ebased catalysts performance in the solar catalytic decomposition of methane for hydrogen and carbon production. **International Journal of Hydrogen Energy** 37: 9645-9655.

_____, R. Utrilla, M.J. Lázaro, R. Moliner, I. Suelves and A.B. García. 2011. Ni- and Fe-based catalysts for hydrogen and carbon nanofilament production by catalytic decomposition of methane in a rotary bed reactor. **Fuel Processing Technology** 92: 1480-1488.

Poirier, M.G. and C. Sapundzhiev. 1997. Catalytic decomposition of natural gas to hydrogen for fuel cell applications. **International Journal of Hydrogen Energy** 22: 429-433.

Qu, F., H. Lin, X. Wu, X. Li, S. Qiu and G. Zhu. 2010. Bio-templated synthesis of highly ordered macro-mesoporous silica material for sustained drug delivery. **Solid State Sciences** 12: 851-856.

Rahman, M., E. Croiset and R. Hudgins. 2006. Catalytic decomposition of methane for hydrogen production. **Topics in Catalysis** 37: 137-145.

Sahin, E., T. Dogu and K. Mürtezaoğlu. 2003. Thermal effects on effectiveness of catalysts having bidisperse pore size distributions. **Chemical Engineering Journal** 93: 143-149.

Scheibe, B., E.B. Palen and R.J. Kalenczuk. 2010. Oxidation and reduction of multiwalled carbon nanotubes preparation and characterization. **Materials Characterization** 61: 185-191

Copyright by Kasetsart University All rights reserved

Shaikhutdinov, S.K., L.B. Avdeeva, O.V. Goncharova, D.I. Kochubey, B.N. Novgorodov and L.M. Plyasova. 1995. Coprecipitated Ni-A1 and Ni-Cu-A1 catalysts for methane decomposition and carbon deposition I. Genesis of Calcined and reduced catalysts. **Applied Catalysis A: General** 126: 125-139.

Shinoda, M., Y. Zhang, Y. Yoneyama, K. Hasegawa and N. Tsubaki. 2004. New bimodal pore catalysts for Fischer-Tropsch synthesis. **Fuel Processing Technology** 86: 73– 85.

Snoeck, J.W., G. F. Froment and M. Fowles. 1997. Kinetic study of the carbon filament formation by methane cracking on a nickel catalyst. **Journal of Catalysis** 169: 250 - 262.

Steinfeld, A., V. Kirillov, G. Kuvshinov, Y. Mogilnykh and A. Reller. 1997. Production of filamentous carbon and hydrogen by solarthermal catalytic cracking of methane. **Chemical Engineering Science** 52: 3599-3603.

Suelves, I., M.J. Lázaro, R. Moliner, B.M. Corbella and J.M. Palacios. 2005. Hydrogen production by thermo catalytic decomposition of methane on Ni-based catalysts: influence of operating conditions on catalyst deactivation and carbon characteristics. **International Journal of Hydrogen Energy** 30: 1555-1567.

Takahashi, R., S. Sato, S. Tomiyama, T. Ohashi and N. Nakamura. 2007. Pore structure control in Ni/SiO_2 catalysts with both macropores and mesopores. **Microporous and Mesoporous Materials** 98: 107-114.

Takenaka, S., H. Ogihara, I. Yamanaka and K. Otsuka. 2001. Decomposition of methane over supported-Ni catalysts: effects of the supports on the catalytic lifetime. **Applied Catalysis A: General** 217: 101-110.

Copyright by Kasetsart University All rights reserved

Takenaka, S., M. Serizawa and K. Otsuka. 2004. Formation of filamentous carbons over supported Fe catalysts through methane decomposition. **Journal of Catalysis** 222: 520-531.

_____, S. Kobayashi, H. Ogihara and K. Otsuka. 2003. Ni/SiO_2 catalyst effective for methane decomposition into hydrogen and carbon nanofibers. **Journal of Catalysis** 217: 79-87

Teabpinyok, N., M. Chareonpanich, S. Samingprai and J. Limtrakul. 2012. pH sensitive structural uniformity of rice husk ash-derived MCM-41 Silica. **Canadian Journal of Chemistry** 90: 881-887.

Venugopal, A., K.S. Naveen, J. Ashok, P.D. Hari, K.V. Durga and K.B.S Prasad. 2007. Hydrogen production by catalytic decomposition of methane over Ni/SiO_2. **International Journal of Hydrogen Energy** 32: 1782-1788.

Lua, A.C. and H.Y. Wang. 2013. Decomposition of methane over unsupported porous nickel and alloy catalyst. **Applied Catalysis B: Environmental** 132- 133: 469-478.

Wang, N., W. Chu, T. Zhang and X.S. Zhao. 2012. Synthesis, characterization and catalytic performances of Ce-SBA-15 supported nickel catalysts for methane dry reforming to hydrogen and syngas. **International Journal of Hydrogen Energy** 37: 19-30.

_____ P., E. Tanabe, K. Ito, J. Jia, H. Morioka, T. Shishido and K. Takehira. 2002. Filamentous carbon prepared by the catalytic pyrolysis of CH_4 on Ni/SiO_2. **Applied Catalysis A: General** 231: 35-44.

Witoon, T., M. Chareonpanich and J. Limtrakul. 2008. Synthesis of bimodal porous silica from rice husk ash via sol–gel process using chitosan as template. **Materials Letters** 62: 1476–1479.

Copyright by Kasetsart University All rights reserved

Yang, R.T. and J.P. Chen. 1989. Mechanism of carbon filament growth on metal catalysts. **Journal of Catalysis** 115: 52-64

Zapata, B., M.A. Valenzuela, J. Palacios and E.T. Garcia. 2010. Effect of Ca, Ce or K oxide addition on the activity of Ni/SiO_2 catalysts for the methane decomposition reaction. **International Journal of Hydrogen Energy** 35: 12091-12097.

Zhang, T. and M.D. Amiridis. 1998. Hydrogen production via the direct cracking of methane over silica-supported nickel catalysts. **Applied Catalysis A: General** 167: 161-172.

_____Y. and K.J. Smith. 2004. Carbon formation thresholds and catalyst deactivation during CH_4 decomposition on supported Co and Ni catalysts. **Catalysis Letters** 95: 7-12.

Zhao, Y., J. Zou, W. Shi and L. Tang. 2006. Preparation and characterization of mesoporous silica spheres with bimodal pore structure from silica/hyperbranched polyester nanocomposites. **Microporous and Mesoporous Materials** 92: 251-258.

Copyright by Kasetsart University All rights reserved

APPENDICES

Copyright by Kasetsart University All rights reserved

Appendix A

Qualitative and Quantitative Results from Gas Chromatography

Copyright by Kasetsart University All rights reserved

Quantitative and Qualitative Results from Gas Chromatography

Gas chromatography was performed in a specially designed instrument. The major instrumental components consisted of a flowing mobile phase, an injector port, a separation column containing the stationary phase, a detector, and a data recording system as shown in Appendix Figure A1. Certain amount of gaseous mixture, 0.5 mL in this research, was injected into gas chromatograph at the injector port and was volatilized in a hot injection chamber before it was transported to the head of the chromatic column. Then, a flow of inert carrier gas (as a mobile phase) swept the injected mixture through a heated column which contained the stationary phase. The gaseous sample moved along the packing column whereas its component gas moved with different flow rates and thus separated into pure component. Before each component exited the instrument, it passed through a detector. The detector sent an electronic signal to the recorder and the analyzed results were printed out.

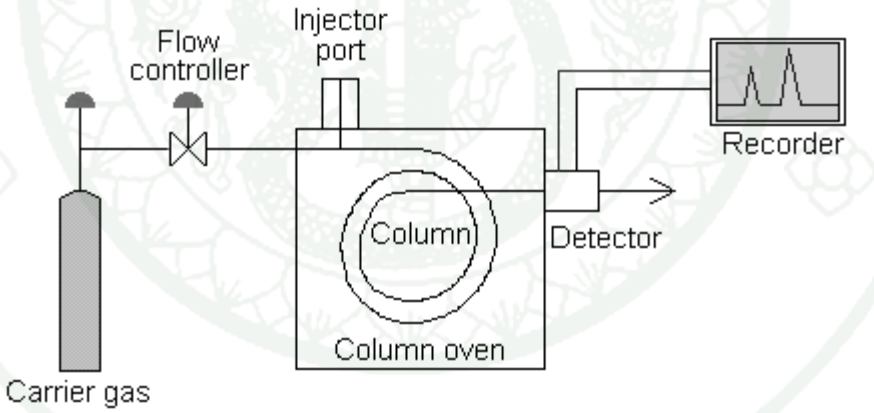

Appendix Figure A1 Schematic diagram of gas chromatograph.

In this work, the quantitative and qualitative data of product composition was obtained from gas chromatography including TCD-GC in the experimental chapter. Before analysis, the condition of operation was set and kept on running for about an hour to stabilize the based line. Certain volume of sample mixture (1.0 mL in this case) was injected into the injection port by gas syringe. After the mixture of sample gas was analyzed, the qualitative and quantitative data were interpreted from the peak

Copyright by Kasetsart University All rights reserved

area obtained from the recorder. The component of injected gas mixture can be identified by using the value of retention time data compared with the retention time received from injected standard gas.

The quantitative analysis of gas samples were obtained from the calibration curves where the correlation between the amount of injected gas sample (mole) and the peak area of gas chromatograms were proposed. The correlation between these parameters (mole and area) was analyzed by a linear regression equation. All the calibration curves for each single standard gas used in this research were shown in Appendix Table A1.

Appendix Table A1 Equation of calibration curves for standard gas and liquid

Substance	Equation	R^2
H_2	mol = 5.0×10^{-12} x area	0.996
CH_4	mol = 2.0×10^{-11} x area	0.999
CO_2	mol = 7.0×10^{-11} x area	0.999
CO	mol = 5.0×10^{-11} x area	0.999
N_2	mol = 4.0×10^{-11} x area	0.999

The calculation for the amount of each component in a standard-gas mixture can be calculated as follows:

$$\text{Amount of component}_i \text{ (mol)} = \frac{V_i \times P}{1000 \times T \times R} \quad \text{(A1)}$$

where V_i = volume of component$_i$ (mL)

P = Pressure of standard gases mixture (atm)

T = Temperature of standard gases mixture (K)

R = Gas constant (0.082057 L·atm/mol·K)

Copyright by Kasetsart University All rights reserved

Appendix B

Conversion and Yield Results

Copyright by Kasetsart University All rights reserved

Conversion and Yield Results

The calculations for the conversion of methane to hydrogen and carbon nanofibers in methane cracking reaction are shown as follows:

Percent of CH_4 conversion:

$$CH_4 \text{ conversion } (\%) = (CH_{4,in} - CH_{4,out})/CH_{4,in} \times 100 \quad \text{(B1)}$$

Percent of hydrogen yield:

$$\text{Yield of hydrogen } (\%) = \frac{\text{moles of hydrogen} \times 100}{2 \times \text{moles of inlet methane}} \quad \text{(B2)}$$

where $CH_{4,in}$ is a mole number of inlet methane

$CH_{4,out}$ is a mole number of outlet methane

Copyright by Kasetsart University All rights reserved

Appendix Table B1 Example of conversion and yield of methane cracking reaction over Ni/BPS-5

Description	Calculation
Methane cracking reaction at T = 500 °C, P = 1 atm	
Inlet: Peak area of CH_4	523400
CH_4 mole (2.0×10^{-11} x area)	1.05×10^{-5} mol
Outlet: Peak area of CH_4	340714
CH_4 mole (2.0×10^{-11} x area)	6.81×10^{-6} mol
CH_4 conversion (%)	35
Peak area of H_2	725777
H_2 mole (5.0×10^{-11} x area)	3.63×10^{-5} mol
H_2 yield (%)	17.33

Copyright by Kasetsart University All rights reserved

Appendix C

Diameter of Crystallite Nickel Oxide Calculation

Copyright by Kasetsart University All rights reserved

Diameter of crystallite nickel oxide calculation

The calculation of crystallite nickel diameter is used Sherer's equation, as shown below:

$$d = \frac{0.9\lambda}{B \cos \theta} \times \frac{180^{o}}{\pi} \quad \text{(C1)}$$

where d is the mean crystallite diameter

λ isthe X-ray wave length (1.54 A°)

B is the full width half maximum (FWHM) of the NiO diffraction peak.

The example of crystallite NiO diameter of Ni/BPS-5 calculation is shown below:

$$B = 0.666°$$

$$d = \frac{0.9 \times 0.154 \text{ (nm)}}{0.666 \times \cos (43.57)} \times \frac{180°}{\pi}$$

$$d = 16.4 \text{ nm}$$

Copyright by Kasetsart University All rights reserved

Appendix D

Effective Diffusion Coefficient Calculation

Copyright by Kasetsart University All rights reserved

Effective Diffusion Coefficient Calculation

In order to calculate the effective diffusion coefficient, the catalysts porosity and tortuosity of catalyst must be investigated and used an equation shown below:

$$D_e = D_{pore}\varepsilon/\tau \quad \text{(D1)}$$

where D_e = effective diffusion coefficients

D_{pore} = diffusivity of methane in pore

ε = porosity

τ = tortuosity

The example of effective diffusion coefficients calculation in Ni/BPS-5 catalyst at temperature of 500 ^{o}C is shown below:

$$1/D_{pore} = 1/D_{AB} + 1/D_K \quad \text{(D2)}$$

where D_{AB} = bulk diffusivity (cm^2/s)

D_K = Knudsen diffusivity (cm^2/s)

$$D_{AB} = \frac{0.001858T^{3/2}[(M_{CH_4}+ M_{N_2})/(M_{CH_4}M_{N_2})]^{1/2}}{[P(\sigma_{CH_4N_2})^2\Omega_D]} \quad \text{(D3)}$$

where T = temperature (K)

M_{CH_4} = molecular weight of CH_4

M_{N_2} = the molecular weight of N_2

P = the total pressure (atm)

$\sigma_{CH_4N_2}$ = the effective collision diameter (Å)

Ω_D = the collision integral

Copyright by Kasetsart University All rights reserved

$$D_{AB} = \frac{0.001858(773)^{3/2}[(16 + 28)/(16x28)]^{1/2}}{[1(3.778)^2 0.7804]}$$

$$= 1.123 \text{ cm}^2/\text{s}$$

$$D_K = 9700 \text{ r } (T/M_{CH_4})^{1/2} \quad \text{(D4)}$$

where r = the pore radius (cm)

$$D_K = 9700 (21.05x10^{-7}) (773/16)^{1/2}$$

$$= 0.142 \text{ cm}^2/\text{s}$$

$$1/D_{pore} = 1/1.1234 + 1/0.1419$$

$$D_{pore} = 0.126 \text{ cm}^2/\text{s}$$

$$D_e = 0.126 (0.7537)/2.0198$$

$$= 0.047 \text{ cm}^2/\text{s}$$

Copyright by Kasetsart University All rights reserved

CIRRICULUM VITAE

NAME : Mr. Chan Tanggarnjanavalukul

BIRTH DATE : September 29, 1989

BIRTH PLACE : Bangkok, Thailand

EDUCATION :

YEAR	INSTITUTE	DEGREE
2012	Kasetsart Univ.	B.Eng. (Chemical)

SCHOLARSHIP : National Research University Scholarship from Center of Advanced studies in Nanotechnology and its Applications in Chemical, Food and Agricultural Industries, Kasetsart University 2012-2014

Copyright by Kasetsart University All rights reserved